

# Warm mid-Pliocene conditions without high climate sensitivity: the CCSM4-Utrecht (CESM 1.0.5) contribution to the PlioMIP2

Michiel L. J. Baatsen<sup>1</sup>, Anna S. von der Heydt<sup>1,2</sup>, Michael A. Kliphuis<sup>1</sup>, Arthur M. Oldeman<sup>1</sup>, and Julia E. Weiffenbach<sup>1</sup>

<sup>1</sup>Institute for Marine and Atmospheric research Utrecht (IMAU), Department of Physics, Utrecht University, Utrecht, The Netherlands.

<sup>2</sup>Centre for Complex Systems Science, Utrecht University, Utrecht, The Netherlands

**Correspondence:** Michiel Baatsen (m.l.j.baatsen@uu.nl)

**Abstract.** We present the Utrecht contribution to the Pliocene Model Intercomparison Project Phase 2 (PlioMIP2), using the Community Earth System Model version 1.0.5 (*CCSM4-Utr*). Using a standard pre-industrial configuration and the *enhanced* PlioMIP2 set of boundary conditions, we perform a set of simulations at various levels of atmospheric pCO<sub>2</sub>. This allows us to make an assessment of the mid-Pliocene reference (Eoi<sup>400</sup>) climate versus available proxy records and a pre-industrial control (E<sup>280</sup>), as well as to determine the sensitivity to different external forcing mechanisms.

We find that our simulated Pliocene climate is considerably warmer than the pre-industrial reference, even under the same levels of atmospheric pCO<sub>2</sub>. Compared to the E<sup>280</sup> case, ~~the simulated climate of our~~ our simulated Eoi<sup>400</sup> climate is on average almost 5°C warmer at the surface. Our Eoi<sup>400</sup> case is among the warmest within the PlioMIP2 ensemble and only comparable to the results of models with a much higher climate sensitivity (i.e. CESM2, EC-Earth3.3, and HadGEM3). This is accompanied by a considerable polar amplification factor, increased globally averaged precipitation and greatly reduced sea ice cover. ~~A primary contribution to this~~ with respect to the pre-industrial reference. In addition to radiative feedbacks (mainly surface albedo, CO<sub>2</sub>, and water vapour) a major contribution to the enhanced Pliocene warmth ~~is likely our~~ in these simulations is the warm model initialisation followed by a long spin-up, as opposed to starting from pre-industrial or present-day conditions. Added warmth in the deep ocean is partly the result of using an altered vertical mixing parametrisation in the Pliocene simulations, but this has a negligible effect at the surface. We find a stronger and deeper Atlantic Meridional Overturning Circulation (AMOC) in the Eoi<sup>400</sup> case, but the associated meridional heat transport is mostly unaffected. In addition to the mean state, we find significant shifts in the behaviour of the dominant modes of variability at annual to decadal timescales. The Eoi<sup>400</sup> ENSO amplitude is greatly reduced (-68%) versus the E<sup>280</sup> one, while the AMOC becomes more variable. There is also a strong coupling between AMOC strength and North Atlantic SST variability in the Eoi<sup>400</sup>, while North Pacific SST anomalies seem to have a reduced global influence with respect to the E<sup>280</sup> through the weakened ENSO.

Copyright statement. TEXT

## 1 Introduction

The Pliocene Model Intercomparison Project Phase 2 (PlioMIP2; Haywood et al. 2016) aims at simulating the mid-Piacenzian Warm Period (mPWP; 3.264 to 3.025 Ma; Haywood et al. 2013a) of the mid-Pliocene using a suite of global numerical climate models. During this interval, the Earth's climate saw warm and relatively stable conditions with atmospheric CO<sub>2</sub> levels similar to those seen today. Being relatively recent in the planet's geologic history, geographical boundary conditions during the mid-Piacenzian were similar to the present. Therefore, the simulated climatic conditions for this specific time interval may serve as a suitable analogue of what to expect in the next century (Burke et al., 2018).

Previous modelling efforts within PlioMIP1 resulted in globally averaged near surface air temperatures between 1.8 and 3.6 °C warmer than those seen today (Haywood et al., 2013b), ~~fee~~ for the mid-Pliocene. The pattern of warming showed clear polar amplification, resulting in a reduced equator-to-pole temperature gradient. However, this reduction was still considerably smaller than suggested by various temperature proxy records and models mostly failed to reproduce the strong warming pattern over the North Atlantic Ocean. The simulated mid-Pliocene warming response was found to be mostly a result of increased atmospheric CO<sub>2</sub>, with surface albedo feedbacks the primary driver behind polar amplification.

In addition to an extended model ensemble, PlioMIP2 offers the use of model boundary conditions from the Pliocene Research, Interpretation and Synoptic Mapping version 4 (PRISM4; Dowsett et al. (2016)). This includes updated estimates of vegetation cover, coastlines, and topography as well as reduced ice sheet cover compared to PRISM3 (Dowsett et al., 2010). As a result, models now show an average warming response of 1.7 to 5.2 °C to these mid-Pliocene boundary conditions. In addition, most models have a mid-Pliocene temperature pattern that better resembles that of proxy reconstructions, particularly with warmer high latitude and North Atlantic regions compared to PlioMIP1 (Haywood et al., 2020).

Here, we present the results of a set of simulations using the Community Earth System Model (CESM) version 1.0.5 within the PlioMIP2 effort. A detailed description of our model configuration, as used in these experiments, is provided in Section 2. This is followed by a general discussion of the PlioMIP2 experimental design and naming conventions in Section 3, together with an overview of our specific set of model experiments. The results of these are presented in Section 4, in which we assess climate sensitivity (4.1), the general mPWP conditions in our simulations (4.2), meridional overturning and heat transports (4.3), a comparison to proxy records (4.4), sensitivity to the applied PlioMIP2 model boundary conditions (4.5), and modes of internal variability in the simulated climate (4.6).

## 2 Model description

### 2.1 The CESM 1.0.5

The Community Earth System Model (Hurrell et al., 2013) is a fully coupled atmosphere-land-ice-ocean general circulation model (GCM) that was developed at the National Center for Atmospheric Research (NCAR) in Boulder, Colorado. For use in palaeoclimate modelling, version 1.0.5 of the CESM is a suitable choice motivated by a trade-off between increasing model complexity and computational cost. This version of the CESM is equivalent to the ~~latest version of~~ last version of its

55 [predecessor](#), the Community Climate System Model (CCSM4; Blackmon et al. 2001; Gent et al. 2011). In other PlioMIP2 studies, our model simulations are therefore referred to as *CCSM4-Utr*.

## 2.2 Atmosphere

The atmospheric component of the CESM is the Community Atmosphere Model (CAM4; Neale et al. 2013) which uses a finite volume dynamical core. The model grid has a nominal horizontal resolution of  $2^\circ$  ( $2.5^\circ \times 1.9^\circ$ ;  $144 \times 96$  grid cells). 26  
60 vertical levels extend upward to 2 hPa, using a hybrid sigma vertical coordinate. In this configuration, the model has a warming response of  $3.17^\circ\text{C}$  per doubling of  $\text{CO}_2$  starting from pre-industrial conditions (Baatsen et al., 2020), which is very similar to the reported value of  $3.14^\circ\text{C}$  by Bitz et al. (2012), and higher than the  $\sim 2.5^\circ\text{C}$  in CCSM3; Kiehl et al. 2006).

In accordance to the PlioMIP2 protocol (Haywood et al., 2016), atmospheric concentrations other than that of  $\text{CO}_2$  are kept at their pre-industrial levels: 671ppb  $\text{CH}_4$ , 270ppb  $\text{N}_2\text{O}$ , and no CFCs. The solar constant is kept at  $1361.27 \text{ Wm}^{-2}$  in all of  
65 our model experiments. Astronomical orbital parameters are set to their present-day configurations for pre-industrial as well as Pliocene simulations, again as suggested by the PlioMIP2 protocol. Atmospheric aerosols are fixed using a pre-industrial climatology ~~-,switching to an adjusted Pliocene climatology for the pre-industrial cases. An adjusted climatology is used for the Pliocene cases,~~ resulting from a Bulk Aerosol Model simulation to incorporate the effect of the PRISM4 boundary conditions.

## 2.3 Land

70 The physical, chemical and biological processes taking place on land are represented in the Community Land Model (CLM4; Oleson et al. 2010; Lawrence et al. 2011). A static rather than dynamic vegetation model is used here to avoid runaway feedback effects, which can become an issue especially in warm greenhouse climates (e.g. dieback of vegetation at low latitudes; Loftson et al. 2014; Herold et al. 2014). Either the pre-industrial biomes or the PRISM4 megabiomes (see also Supplementary Table S1) are translated into fractions of the corresponding CLM4 plant functional types (PFTs), from which a set of monthly forcing  
75 files is ultimately used in the model. Fresh water runoff is treated by a simple river routing scheme, in which all runoff is transported to one of the surrounding 8 model grid cells until the ocean is reached. The direction is determined by the local topography gradient and manually adjusted where the runoff scheme would otherwise form closed loops. Within the CLM4, land ice is implemented as bare soil with a given surface elevation and its specific surface properties (e.g. albedo, evaporation and run-off). As suggested by Haywood et al. (2016), the static land ice configuration used here is based on the results of  
80 previous modelling efforts in PlioMIP1. This includes a greatly reduced Greenland Ice Sheet compared to the present day, as well as an absent West-Antarctic Ice Sheet.

## 2.4 Ocean

The CESM1 uses the Los Alamos National Laboratory (LANL) Parallel Ocean Program version 2 (POP2; Smith et al. 2010) for the ocean model component. The standard configuration is applied here, with a nominal  $1^\circ$  ( $1.25^\circ \times 0.9^\circ$ ) horizontal resolution  
85 on a curvilinear grid placing the northern pole over Greenland. The POP2 model is set up with 60 vertical layers of varying

thickness between 10m near the surface and 250m at greater depth. Horizontal viscosity is considered anisotropic (Smith and McWilliams, 2003) and horizontal tracer diffusion follows the parameterisation of Gent and McWilliams (1990). The model further uses the KPP-scheme to determine vertical mixing coefficients (Large et al., 1994). More information and discussion on the ocean model physics and parameterisations can be found in Danabasoglu et al. (2008, 2012).

90 The sea ice component consists of the LANL Community Ice Code version 4 (CICE4; Hunke and Lipscomb 2008). For simplicity, sea ice only forms when the sea surface cools down to  $-1.8^{\circ}\text{C}$ , after which its dynamical behaviour (e.g. melt and advection) is treated by the model specifically.

In all of our model experiments [considered here](#), tidal mixing and overflow parameterisations are switched off. The pre-industrial reference uses a uniform background vertical diffusivity, set at  $0.16\text{ cm}^2\text{s}^{-1}$ . In contrast, the Pliocene simulations  
95 have a vertically varying background vertical diffusivity determined by:  $\kappa_w = vdc1 + vdc2 \tan^{-1}(|z| - dpth)linv$ , where:  $vdc1 = 0.524\text{ cm}^2\text{s}^{-1}$ ,  $vdc2 = 0.313\text{ cm}^2\text{s}^{-1}$ ,  $dpth = 1000\text{m}$  (the reference depth) and  $linv = 4.5 \cdot 10^{-3}\text{ m}^{-1}$  (the inverse scaling length).  $\kappa_w$  thus varies between  $0.1\text{ cm}^2\text{s}^{-1}$  at the surface and  $1\text{ cm}^2\text{s}^{-1}$  at the bottom of the ocean. [We The latter is done to be consistent with other palaeo-climate simulations using the same model set-up, e.g. Baatsen et al. \(2020\). To study the effect of the different mixing parameter settings, we](#) carry out an additional pre-industrial simulation [with using](#) the same oceanic  
100 configuration [used as](#) for the Pliocene cases (see Section 3), ~~to study the effect of these altered parameter settings compared to the standard configuration (~~ Figures S4 ~~and S8~~, [S7, and S9](#) in the supplementary material). The enhanced vertical mixing in the deep ocean results in an overall warming of the deep ocean at the expense of a slight cooling at upper levels. Near the surface, ~~however, very little change is~~ [globally averaged temperatures are near identical but some regional changes are](#) seen as a result of the different vertical mixing schemes. ~~Another~~ [For completeness, another](#) pre-industrial simulation ~~in which we~~  
105 ~~turn on is carried out using the standard configuration in which~~ the tidal mixing and overflow parameterisations ~~shows that their combined effect are~~ [switched on. The results show no significant temperature differences seen at any depth level and thus suggests that the combined effect of these parameterisations](#) is negligible within the scope of this study and the specific model configuration used here ~~(i. e. no significant temperature differences seen at any depth level).~~

### 3 PlioMIP2 experiments

#### 110 3.1 PRISM4 boundary conditions

Following the methodology outlined by Haywood et al. (2016), we perform a set of pre-industrial and Pliocene simulations using the CESM1.0.5. As we carry out a number of different model experiments, we will refer to these as either *pre-industrial* or *Pliocene* (rather than mid-Piacenzian) regardless of atmospheric  $\text{pCO}_{22}$ . For Pliocene cases we incorporate the set of enhanced boundary conditions based on the PRISM4 (Dowsett et al., 2016). These include altered topography and bathymetry, coastlines,  
115 land surface properties (i.e. vegetation, soil type and ice sheet coverage) and atmospheric composition with respect to pre-industrial conditions. Our Pliocene model geography is implemented by applying the PRISM4 topography and bathymetry anomalies to the pre-industrial reference, after re-gridding onto the specific model resolution used here. The PRISM4 land-sea mask is then also interpolated onto the model grid and applied to the Pliocene model geography. A manual check of the entire

model grid is done, altering land and ocean cells where needed and making sure that any marine passages are either at least 2  
120 cells wide when open, or closed if needed. The resulting model geography for the Pliocene simulations is shown in Figure 1  
and compared to that of the pre-industrial reference. Corresponding vegetation cover and aerosol optical depth can be found in  
Figure S1 of the supplementary material.

Some of the main aspects of the Pliocene model geography with respect to the pre-industrial reference include a closure of

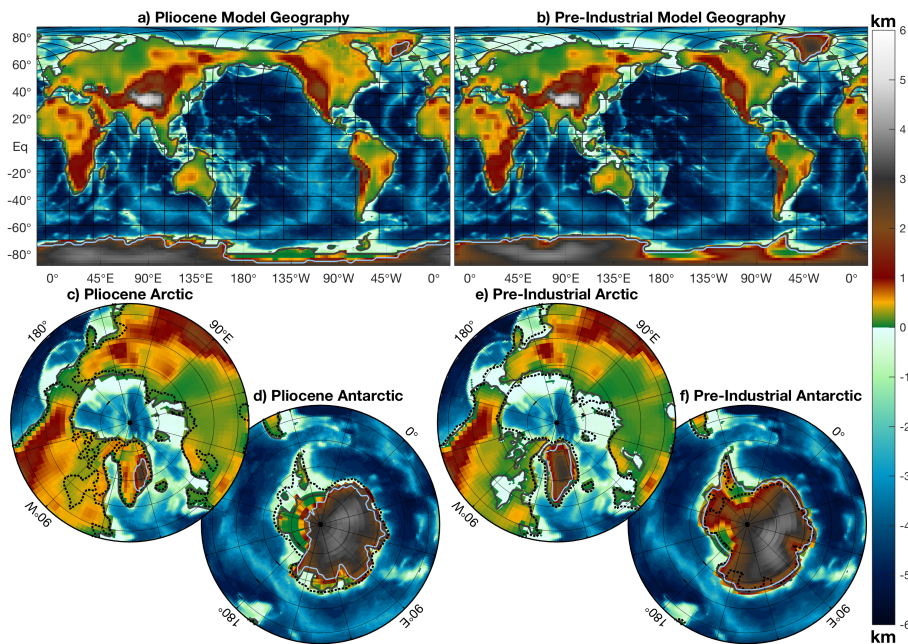


**Figure 1.** Model geography as applied in our different **a)** Pliocene and **b)** pre-industrial cases. Both the bathymetry and topography are shown at the native model grid, with the CAM4 rectangular grid superimposed on the finer POP2 curvilinear grid wherever the land fraction is at least 0.5 (also indicated by the thick grey contour line). The light blue contour line shows the extent of land ice, as imposed by the land use distribution. **c,e** Northern and **d,f** Southern polar stereographic views Pliocene and pre-industrial model geography.

both the Bering Strait and Northwest Passage, making the Arctic Ocean much more isolated from the other ocean basins.  
125 Prior to large-scale glaciation on the Northern Hemisphere during the Quaternary period, a considerable part of the northern  
Eurasian continental shelf as well as the Hudson Bay area were exposed. Furthermore, large parts of the Maritime Continent  
are also considered to have been above sea level during the mid-Pliocene. Finally, there was significantly less land ice cover  
compared to the present, covering only part of Southeast Greenland and East Antarctica. Note that the Gibraltar straight is  
open while the Panama Gateway is closed in all of our simulations (this is obscured in the figures by the superposition of the  
130 atmospheric model grid onto the bathymetry).

### 3.2 Experimental design and model spin-up

In accordance with the PlioMIP2 guidelines we performed both a pre-industrial reference and Pliocene control *core* simulation, which are referred to as  $E^{280}$  and  $Eoi^{400}$ , respectively (following the naming conventions of Haywood et al. 2016). In addition to the pre-industrial reference we added two *climate sensitivity* simulations, with a doubling ( $E^{560}$ ) and quadrupling ( $E^{1120}$ ) of atmospheric  $CO_2$ . Two more sensitivity experiments were added to the Pliocene control, in which we applied pre-industrial ( $Eoi^{280}$ ) and doubled ( $Eoi^{560}$ )  $CO_2$  levels. This enables us to make a complete assessment of the model's sensitivity to either Pliocene boundary conditions or radiative forcing, for the full range of possible reference states. Besides altered model boundary conditions, the Pliocene simulations differ from the pre-industrial ones as a result of the oceanic vertical mixing parameters. Another *mixing sensitivity* experiment is thus added as a continuation from the  $E^{280}$  simulation, using the same ocean mixing configuration for the ocean as in the Pliocene cases, referred to as  $E^{280,P}$ . Results of an additional (500-year) pre-industrial simulation with tidal mixing and overflow parameterisations switched on ( $E^{280,S}$ ), are not used besides a technical robustness check and therefore not considered. See also Table 1 for an overview of the different simulations.

The pre-industrial reference simulation is initialised using present-day (year 2000) temperature and salinity fields from the

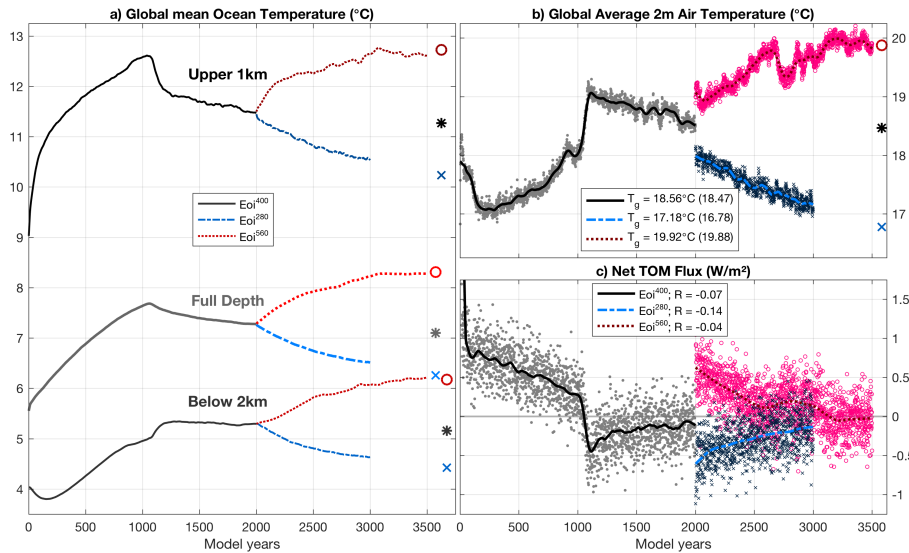


**Figure 2.** Time series of globally averaged temperatures for the entire length of our 3 different Pliocene simulations:  $Eoi^{400}$  (black),  $Eoi^{280}$  (blue), and  $Eoi^{560}$  (red). Shown are the **a)** upper (dark), deep (medium), and full depth (light) ocean temperature, **b)** near surface air temperature, and **c)** globally averaged top of model (TOM) net radiative flux. Thick lines in b,c show the corresponding time series after applying a 100-year smoothing mask. The estimated equilibrium temperatures are indicated at the end in a,b, using large markers and the same colour convention. The globally averaged, mean temperature ( $T_g$  in b) and net radiative flux ( $R$  in c) over the last 100 years are added in the legends (bracketed values for the estimated equilibrium).

PHC2 dataset (Steele et al., 2001). As these are slightly warmer than pre-industrial conditions, a long spin-up of  $>3000$  years is carried out to equilibrate the full ocean. The remaining drift of volume-weighted average ocean temperature at the end of

this simulation is brought down to  $\sim 10^{-4}$  K/year (Table 1). In contrast, the Pliocene control simulation is started with a highly idealised ocean temperature and salinity distribution. The initial temperature is horizontally homogeneous while salinity is set to 35psu globally. The vertical profile of temperature decreases downward between 15°C at the surface and 4°C in the deep ocean. We thus apply ~~the same initial conditions as~~ similar initial conditions to those used in the Eocene simulations of Baatsen et al. (2020), ~~with a downward adjustment of~~ but with cooler deep ocean temperatures. The latter is done to match the volume-integrated, global ocean temperatures of Rosenbloom et al. (2013), who used the CCSM4 to model the mid-Pliocene within the PlioMIP1. This way, we start the model with a total ocean heat content similar to previously found Pliocene conditions using a very similar model configuration. Still, we perform 2000 model years of spin-up to acquire a well-equilibrated oceanic state for our Pliocene control. An overview of the temperature evolution during this spin up along with the top of model radiative imbalance can be found in Figure 2, ~~which shows substantial temperature adjustments. After an initial warming phase, an abrupt change in temperature trends is seen at  $\sim 1000$  years into the Eoi<sup>400</sup> simulation. This is the result of a shift in the oceanic circulation, associated with the formation of deep overturning cells in the North Atlantic and Southern Ocean. These act to mix heat from the upper into the deep ocean, but also increase high latitude temperatures through enhanced meridional heat transport (see also Figure 7). Similar temperature trends were seen by Chandan and Richard Peltier (2017), especially considering their~~ POPI type vertical mixing simulations, in which they implement an identical ocean set-up to our mid-Pliocene cases (and E<sup>280,P</sup>) yet with a cooler initial state. Additional information on the spin-up behaviour of the set of model simulations presented here can be found in Figures S2 and S3 of the supplementary material.

All three pre-industrial sensitivity experiments are started from the equilibrated state at the end of the E<sup>280</sup> control simulation. The E<sup>560</sup> and E<sup>1120</sup> cases are continued for another 1000 and 2000 model years, respectively, while the E<sup>280,P</sup> is continued for ~~2000~~ 2300 model years (see also Figure S4 of the supplementary material). The E<sup>560</sup> and E<sup>1120</sup> simulations still have substantial drifts in deep ocean temperature, but much less near the surface. Using the transient behaviour, however, we can estimate the actual equilibrium temperatures (see section 3.3) and therefore the climate sensitivity of the model within this specific set-up. In the global average, the effect of altered ocean mixing parameters is quite clear: there is no temperature change at the surface, but the upper ocean cools slightly while the deep ocean warms. The more efficient downward mixing of heat leads to an average warming of the total water column (by  $\sim 0.8^\circ\text{C}$ ) in the extrapolated equilibrium. The Eoi<sup>280</sup> and Eoi<sup>560</sup> simulations are initialised from the Eoi<sup>400</sup> control at year 2000 and continued for 1000 and 1500 years, respectively. As their initial radiative forcing is relatively small compared to a full doubling of CO<sub>2</sub>, ~~they acquire a small temperature drift relatively quickly~~ it does not take as long for the temperature drifts to become small. The Eoi<sup>560</sup> simulation is longer compared to the Eoi<sup>280</sup> one as it was showing substantial internal variability after about 700 years owing to large (i.e.  $>10\text{Sv}$ ) fluctuations in the Atlantic Meridional Overturning Circulation strength (~~see also~~ Figure S5 in the supplementary material).

### 3.3 Data analysis and methods

Within the PlioMIP2 ~~data database, model fields~~ from the last 100 model years of the E<sup>280</sup>, E<sup>560</sup>, Eoi<sup>280</sup>, Eoi<sup>400</sup>, and Eoi<sup>560</sup> case are publicly available. We use the same 100 years here for our analyses and to calculate time means in order to best match the results of other studies. Some more extensive data time series are considered as well, but only when noted specifically. The

180 overview of modelled atmospheric and oceanic conditions given in Section 4.2 is based on climatologies using the same 100  
years at the end of the E<sup>280</sup> and Eoi<sup>400</sup> runs. From the E<sup>280,P</sup> simulation we use 200-year averages instead (i.e. 4400–4600) as  
it exhibits some long-term fluctuations (see Figure S4 in the supplementary material). In addition to the model data presented  
here, we make use of ~~the ERSST dataset (Huang et al., 2017), satellite-based passive microwave sea ice concentration data~~  
185 ~~by the 1870–1899 mean SST, which is calculated from the ERSST version 5 monthly fields. We also use~~. We consider  
1988–2000 mean sea ice concentration, excluding more recent years in which a rapid decline of Arctic sea ice was observed.  
We also use mid-Pliocene (more specifically the KM5c interglacial period) SST proxies from McClymont et al. (2020). This  
record includes absolute SST estimates using the newly calibrated U<sub>37</sub><sup>K'</sup> and Mg/Ca proxies, as well as SST anomalies which  
are calculated with respect to the 1870–1899 ERSST reanalysis (Huang et al., 2017).

190 In addition to direct climatological or annual mean fields at the end of each simulation, we also present a number of esti-  
mated equilibrium values using the complete time series of ~~a particular model run~~ the according temperatures and radiative  
fluxes. Based on the method of Gregory et al. (2004), we linearly extrapolate the trend of a specific temperature measure to-  
wards a net zero top of model (TOM) radiative flux. It should be noted that the original technique of Gregory et al. (2004) is  
195 designed to estimate equilibrium temperatures from relatively short (~50 years) simulations following an initial perturbation.  
Using a much longer time series, we do include the effects of slower ~~feedbacks such as deep~~ (e.g. ocean thermal adjustment  
and  
Baatsen et al. 2020; Farnsworth et al. 2019) and nonlinear (e.g. clouds; Bloch-Johnson et al. 2015; Knutti and Rugenstein 2015  
) feedbacks and therefore can acquire a better estimate of the actual equilibrium temperature (but also require a much longer  
simulation time). The net TOM radiation is calculated by subtracting the (surface-weighted) globally averaged net outgoing  
200 longwave flux from the net incoming shortwave flux. A visualisation of the standard procedure for globally averaged near  
surface air temperature in the Eoi<sup>280</sup>, Eoi<sup>400</sup>, and Eoi<sup>560</sup> cases can be found in Figure S2 of the supplementary material. An  
extension towards upper (<1km), deep (>2km) and full-depth ocean temperatures from all of our simulations is also provided  
in Figure S3. As shown by Gregory et al. (2004), the equilibration of the globally averaged near surface air temperature from  
an initial shock in radiative forcing becomes linear as a function of the net TOM radiative flux. However, their simulations  
205 use a slab ocean rather than a full-depth ocean model component. Using our model configuration, the equilibration is slightly  
non-linear instead, especially at the start of the simulation (see also Baatsen et al. 2020). Therefore, we exclude the first 100 or  
250 years of data from this analysis for atmospheric or oceanic temperatures, respectively.

To get a quantitative assessment of the temperature contributions from different components in the radiative balance between  
210 our sensitivity simulations, we repeat the analysis of Hill et al. (2014) using an energy balance framework similar to Lunt et al. (2021); Hein  
. We adopt the radiative balance equation as:

$$\underline{S(1 - \alpha_p) + H + F_{cloud} + F_{CO_2} = \epsilon\sigma\tau^4,}$$



215 where  $S$  is the incoming solar radiation,  $\alpha_p$  the planetary albedo,  $H$  the meridional heat transport,  $F_{cloud}$  the cloud radiative forcing,  $F_{CO_2}$  the radiative forcing resulting from a doubling of atmospheric  $pCO_2$ ,  $\epsilon$  the emissivity,  $\sigma$  the Stefan-Boltzmann constant, and  $\tau$  the surface temperature. This equation can be rearranged to determine the surface temperature, using the annual mean model fields from each simulation. The temperature effect of a single component between 2 different simulations can then be estimated by the temperature difference by adjusting this component in the energy balance equation. Note that in the reference temperature, both  $F_{cloud}$  and  $F_{CO_2}$  are 0. In contrast to Lunt et al. (2021), we consider the full 2D fields and then take the zonal average of the resulting temperature difference. We also include the effects of surface albedo, shortwave/longwave  
220 cloud forcing and  $CO_2$  as components in the energy balance.

In our analysis of the ocean circulation, we consider the barotropic stream function (BSF) and meridional overturning stream function (MSF). Both of these are calculated from the monthly averaged horizontal flow fields and integrated as a function of latitude and either depth (BSF) or longitude (MSF), starting from the southern pole located on Antarctica. ~~These analyses~~  
225 ~~are again using the~~ The last 100 years of ~~model output from each of our simulations~~ each simulation are again used for the calculation of the BSF, but the last 500 years are used for the MSF (to avoid a possible influence of centennial-scale variability). From the MSF, we also determine the strength of the Atlantic meridional overturning circulation (AMOC). This is defined as the maximum of the overturning stream function below 1000m and north of  $30^\circ S$ , using only the flow field in the Atlantic Ocean.

230 We look at the temporal variability of SSTs through El Niño Southern Oscillation (ENSO), Atlantic/Pacific (Multi-)Decadal Variability (AMV/PMV) and the AMOC time series. ENSO is characterised by the Niño indices, taking the monthly average SST anomaly over  $0-10^\circ S$ ,  $90-80^\circ W$  (Niño 1+2) and  $5^\circ N-5^\circ S$ ,  $170-120^\circ W$  (Niño 3.4). To capture ENSO variability on decadal time scales as well, we use 200 rather than 100 years of monthly SST data. We subtract the 12-monthly climatological  
235 mean and apply a linear de-trending to each model grid point. The resulting Niño time series are then treated with a 5-month running mean.

The calculation of AMV/PMV indices requires the use of empirical orthogonal functions (EOFs), using 500 years of annual mean SST data as these processes occur on longer timescales (see e.g. Deser et al. 2012; Trenberth and Shea 2006, and <https://climatedataguide.ucar.edu/data-type/climate-indices>; date of last access: 17/08/2021). We apply a local de-trending to  
240 annual SST time series at each grid point by subtracting a 200-year smoothing spline. We then determine the first three spatial EOFs of the resulting SST anomalies for the North Atlantic ( $10-70^\circ N$ ) and North Pacific ( $20-60^\circ N$ ) Ocean. The AMV mode is then determined as the EOF of which the time series correlates best with the North Atlantic average SST ~~to not select a mode that is~~ (rather than the first EOF, as the variability may be dominated by e.g. ENSO or PMV). The PMV is simply the dominant EOF in the North Pacific Ocean, obtained from the annual SST anomalies. Patterns of SST variability corresponding  
245 to these modes can then be obtained by correlating the local SST anomalies to each of the specific mode time series.

We perform a spectral analysis of the different modes of variability, using a multi-tapered method (MTM) as it is more suitable for climatic time series of limited length (Ghil et al., 2002). This method is based on a standard Fourier analysis, but uses

**Table 1.** Overview of globally averaged observables and equilibration measures for all of our simulated cases, including simulation length (+ denotes a continuation from the above control case), mean annual 2m air temperature (MAT), average tropical temperature  $MAT_T$ , average polar temperature  $MAT_P$ , mean annual precipitation (MAP), top of model net radiative flux ( $R_{TOM}$ ), sea surface temperature (SST), full depth ocean temperature (OT), and ocean temperature drift. Subscript  $e$  denotes estimated equilibration values.

Measure Simulation	Length (years)	MAT (°C)	$MAT_e$ (°C)	$MAT_T$ (°C)	$MAT_P$ (°C)	MAP (m yr <sup>-1</sup> )	$R_{TOM}$ (W m <sup>-2</sup> )	SST (°C)	OT (°C)	$OT_e$ (°C)	OT Drift (10 <sup>-4</sup> K yr <sup>-1</sup> )
<b>E<sup>280</sup></b>	<b>3100</b>	<b>13.85</b>	<b>13.82</b>	<b>25.32</b>	<b>-22.51</b>	<b>1.046</b>	<b>-0.002</b>	<b>18.42</b>	<b>3.04</b>	<b>3.04</b>	<b>-1.03</b>
E <sup>280,P</sup>	+2700 +2200	13.87	13.83	25.28	-22.30	1.044	+0.016	18.40	3.61	3.65	+1.56
E <sup>560</sup>	+1000	16.54	16.75	27.25	-16.94	1.092	+0.187	20.23	4.14	5.14	+6.18
E <sup>1120</sup>	+2000	19.86	20.16	29.52	-9.52	1.156	+0.214	22.66	6.66	8.15	+6.89
<b>Eoi<sup>400</sup></b>	<b>2000</b>	<b>18.54</b>	<b>18.47</b>	<b>28.02</b>	<b>-10.09</b>	<b>1.181</b>	<b>-0.073</b>	<b>21.89</b>	<b>7.28</b>	<b>7.09</b>	<b>-1.64</b>
Eoi <sup>280</sup>	+1000	17.17	16.78	27.01	-12.98	1.154	-0.139	20.86	6.53	6.25	-3.19
Eoi <sup>560</sup>	+1500	19.91	19.88	29.01	-7.21	1.208	-0.042	22.97	8.28	8.27	+0.76

tapers to limit cut-off effects at the edges of the respective time series. We apply this technique, using 3 tapers and a bandwidth parameter of 2. All of the resulting power spectra are tested against a red noise null hypothesis, using 10.000 random AR1 surrogate time series. The median of these red noise power spectra is used to normalise those of the corresponding modes of variability, making the latter more easy easier to interpret as well as consider their statistical significance using 90%, 95%, and 99% confidence levels. Finally, we also correlate the time series of different modes: AMV, PMV, AMOC and ENSO (now using 500 years of annual SST anomalies for the latter as well, rather than 200 years of monthly SST anomalies). These correlations are considered significant when their corresponding p-value is less than 0.05 (i.e. white noise null hypothesis).

255

## 4 Results

### 4.1 Global averages and climate sensitivity

An overview of globally averaged temperatures, drifts and radiative balance at the end of each of our model simulations is provided in Table 1. These values, including some additional metrics of the vertical thermal distribution of the ocean, are visualised in Figure 3. Throughout the different cases, we see a consistent globally averaged equilibrium warming of  $\sim 3^\circ\text{C}$  per  $\text{CO}_2$  doubling in the near surface atmosphere. This warming response reduces slightly to  $\sim 2.5^\circ\text{C}$  in the ocean. The globally averaged sea surface temperature (SST) only increases by  $\sim 2.1^\circ\text{C}$  per  $\text{CO}_2$  doubling, as a result of. In addition to different surface feedbacks over land versus sea, the inhomogeneous distribution of land/sea (i.e. more land at high latitudes) acts to further differentiate between the average temperature over the land and sea surface. There is some nonlinear response towards

260

265 higher CO<sub>2</sub> concentrations, [consistent with e.g. Lunt et al. \(2021\); Baatsen et al. \(2020\); Caballero and Huber \(2013\)](#), which is closely related to the corresponding radiative forcing in the model. Starting from the pre-industrial reference, a single CO<sub>2</sub> doubling results in an initial perturbation of 3.49 W m<sup>-2</sup> while a quadrupling of CO<sub>2</sub> induces 7.93 W m<sup>-2</sup>, meaning that the radiative forcing of 4×CO<sub>2</sub> is 2.27 (rather than 2) times that of 2×CO<sub>2</sub> ([Baatsen et al., 2020](#)) ([Baatsen et al., 2020; Etminan et al., 2016](#)). Using the corresponding deviation of the globally averaged near surface air temperature (2.93°C and 6.34°C in the E<sup>560</sup> and  
270 E<sup>1120</sup>, respectively), we find a climate sensitivity parameter of 0.80–0.84 K W<sup>-1</sup> m<sup>2</sup>. Using the E<sup>1120</sup> extrapolated temperature, we report an estimated equilibrium climate sensitivity (ECS) of 3.17°C per CO<sub>2</sub> doubling, noting the nonlinearity towards higher pCO<sub>2</sub>. Comparing the Eoi<sup>560</sup>- Eoi<sup>280</sup> temperatures, we find a difference of 3.2°C, indicating a similar ECS between the modelled pre-industrial and Pliocene states. The observation that the Pliocene ECS tends towards the higher regime of pre-industrial (i.e. E<sup>1120</sup>- E<sup>560</sup> rather than E<sup>560</sup>- E<sup>280</sup>) suggests that the nonlinearity in ECS is a function of the reference temperature  
275 rather than pCO<sub>2</sub>, as the Eoi<sup>280</sup> temperatures are comparable to the E<sup>560</sup> ones.

Strikingly, the applied mid-Pliocene model boundary conditions result in an average warming similar to a doubling of atmospheric pCO<sub>2</sub> regardless of background CO<sub>2</sub> level. Looking at the upper (<1000m) versus deep (>2000m) ocean average temperatures in Figure 3, the offset between pre-industrial and mid-Pliocene conditions seems depth-dependent. While the upper ocean is about 2°C warmer in our mid-Pliocene simulations, the deep ocean is over 3.5°C warmer compared to the  
280 pre-industrial cases. [Taking Much of this warming pattern can be explained by taking](#) into account the extrapolated equilibrium temperatures of the E<sup>280,P</sup> simulation as well [, the \(crosses in Figure 3, see also Figure S4\). The](#) vertical redistribution of heat can be [mostly](#) attributed to the [altered-vertical](#) mixing parameters in the mid-Pliocene model set-up. After correcting the [temperature-pre-industrial temperatures with the E<sup>280,P</sup>- E<sup>280</sup>, difference, the average](#) offsets between pre-industrial and mid-Pliocene simulations [, the global average](#) again closely resembles that of a CO<sub>2</sub> doubling [\(i.e. ~2.5°C; bracketed values](#)  
285 [in Figure 3\)](#). A more detailed look into the distribution of different temperature responses to [either external radiative forcing or only a change in atmospheric pCO<sub>2</sub> or other](#) model boundary conditions is presented in Section 4.5.

Compared to the E<sup>280</sup> pre-industrial reference, the simulated climate of our Eoi<sup>400</sup> mid-Pliocene control is on average almost 5°C warmer at the surface. This is accompanied by a 13% increase in mean annual precipitation and a considerable polar amplification factor. The latter is found by comparing the change in average polar (>66.5°N/S) to tropical (<23.5°N/S) temperature: MAT<sub>P</sub>/MAT<sub>T</sub> between different cases. This gives a polar amplification factor of 3.11 and 3.17 for the E<sup>560</sup> and E<sup>1120</sup>, respectively, compared to the E<sup>280</sup>. A slightly smaller value of 2.85 is found between the Eoi<sup>560</sup> and Eoi<sup>280</sup>, but a much larger polar amplification factor of 4.75 is seen between the Eoi<sup>400</sup> and E<sup>280</sup>, including the effect of changing the model boundary conditions. This value increases further to 5.78 (Eoi<sup>280</sup>- E<sup>280</sup>) or 5.42 (Eoi<sup>560</sup>- E<sup>560</sup>) between Pliocene and pre-industrial cases at equal atmospheric pCO<sub>2</sub>, indicating a strongly enhanced temperature response towards high latitudes to the applied Pliocene  
295 model boundary conditions.

As shown in Figure 3 and Table 1, the full depth average of the oceans is about 2.5°C warmer in our Pliocene simulations compared to the equivalent pre-industrial case at equilibrium. Differences in land ice cover and vegetation type, but also snow and sea ice coverage provide a substantial contribution to the modelled Pliocene warmth (see also Table S2 in the supplementary material). Shortwave surface fluxes alone account for a ~6 W m<sup>-2</sup> net forcing in the globally averaged radiative balance,

300 comparing Pliocene to pre-industrial cases at equal  $p\text{CO}_2$  ( $E_{\text{oi}^{280}} - E^{280}$ :  $6.6 \text{ W m}^{-2}$ ;  $E_{\text{oi}^{560}} - E^{560}$ :  $5.4 \text{ W m}^{-2}$ ). The responsible surface albedo feedback thus plays a primary role, decreasing slightly towards a warmer reference state. Although small, shortwave cloud feedbacks ( $E_{\text{oi}^{280}} - E^{280}$ :  $-1.2 \text{ W m}^{-2}$ ;  $E_{\text{oi}^{560}} - E^{560}$ :  $0 \text{ W m}^{-2}$ ) counteract the reduced effect of surface albedo towards warmer states, helping to explain why we see a similar climate sensitivity across all of our model cases. Longwave radiative fluxes play a similar role to enhance Pliocene warmth in our simulations, mainly through the lapse rate and

305 water vapour feedback. A warmer ocean surface and atmosphere lead to an increase in the total column water vapour, which acts as a greenhouse gas. In contrast to shortwave fluxes, this effect becomes larger towards warmer conditions ( $E_{\text{oi}^{280}} - E^{280}$ :  $11.4 \text{ W m}^{-2}$ ;  $E_{\text{oi}^{560}} - E^{560}$ :  $12.1 \text{ W m}^{-2}$ ), but is again mitigated by small longwave cloud feedbacks ( $E_{\text{oi}^{280}} - E^{280}$ :  $0.7 \text{ W m}^{-2}$ ;  $E_{\text{oi}^{560}} - E^{560}$ :  $0.2 \text{ W m}^{-2}$ ).

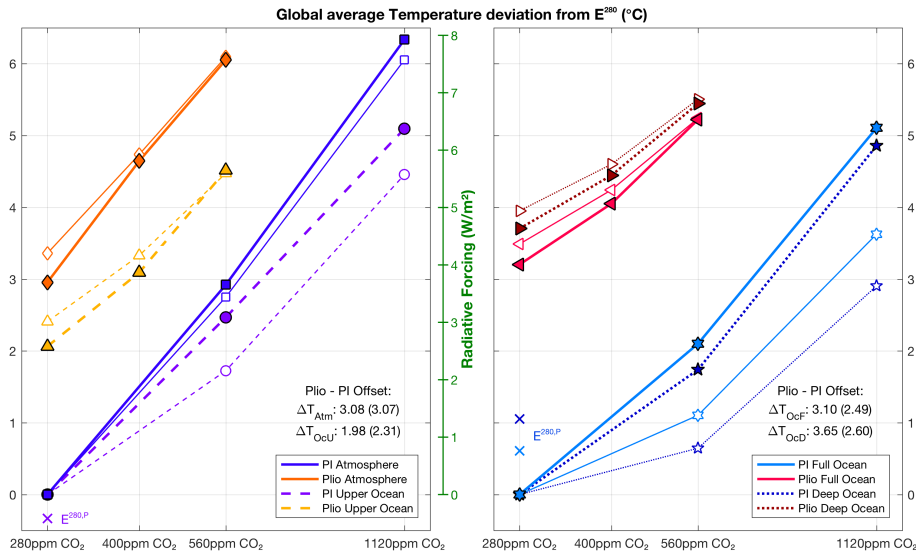


**Figure 3.** Overview of global average temperature in all of our different pre-industrial and Pliocene cases, compared to the  $E^{280}$ . Open markers, connected by thin lines, show the time mean at the of each simulation. Filled markers, connected by thick lines, show the corresponding equilibrium values. Cool colours are used for pre-industrial (*PI*) cases, warm colours for the Pliocene (*Plio*) ones. We consider 4 different temperature measures: near surface air temperature, upper ocean, full ocean, and deep ocean surface/volume weighted averages. Crosses indicate extrapolated temperatures from the  $E^{280,P}$  case. Pliocene–pre-industrial offset values are given, determined by the mean temperature difference between cases at equal  $\text{CO}_2$  (using a log interpolation between 280 and 560 ppm, to estimate the missing  $E^{400}$ ). A similar offset, corrected for the difference between the  $E^{280}$  and  $E^{280,P}$ , is shown between brackets.

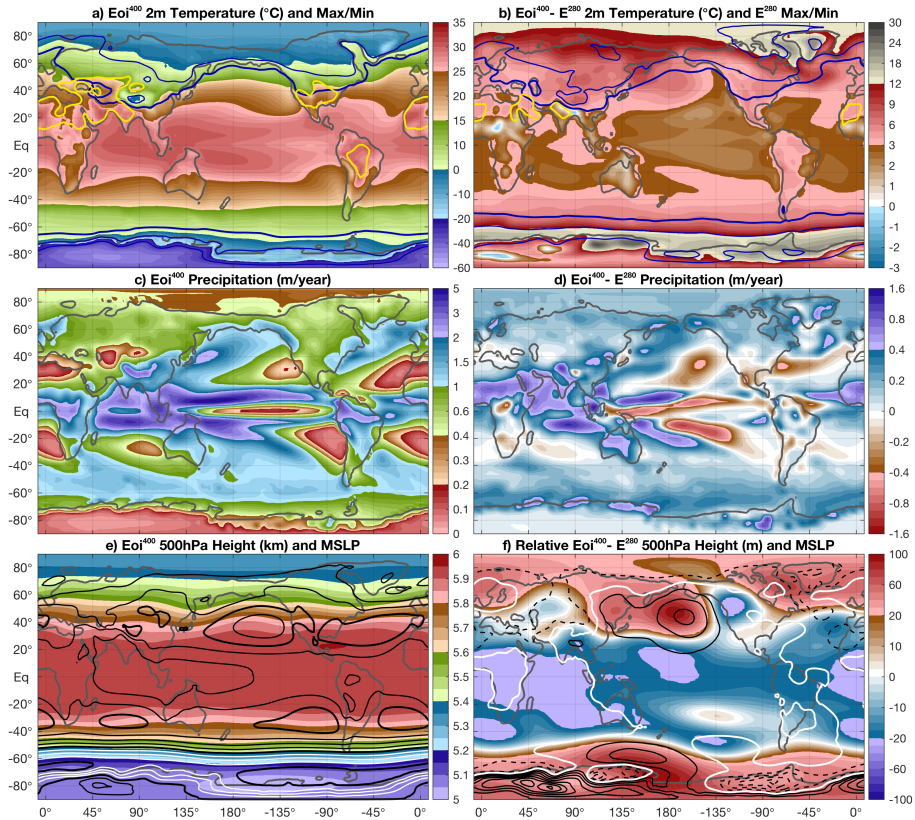


**Figure 4.** Annual mean atmospheric ~~observables~~ model fields from our  $Eoi^{400}$  case (left) and the  $Eoi^{400} - E^{280}$  difference. **a,b)** Near surface (2m) air temperature (shading), warmest month mean maximum (contours; white: yellow contour at  $40^{\circ}\text{C}$ ), and coldest month mean minimum (contours; blue  $\div$  contours at  $0^{\circ}\text{C}$ , cyan:  $-10$ - $20^{\circ}\text{C}$ , magenta:  $-20$  and  $-40^{\circ}\text{C}$ ). Contours in (a):  $Eoi^{400}$ ; in (b)  $E^{280}$ . **c,d)** Precipitation (m/year), differences in (d) are smoothed over land. **e)** Height of the 500hPa pressure level (shading) and mean sea level pressure (MSLP; contours every 5hPa, black  $\leq 1000$  hPa, white  $< 1000$ hPa, thick line every 20hPa). **f)** 500hPa height difference with respect to the global average  $Eoi^{400} - E^{280}$  value (i.e. 96m), contours are used for MSLP (every 2 hPa, solid  $> 0$ , dashed  $< 0$ , thick white line at 0hPa).

## 4.2 Simulated mid-Pliocene Conditions

### 310 4.2.1 Atmosphere

Looking at the annual mean near surface air temperature in the  $Eoi^{400}$  versus  $E^{280}$  case (Figure 4 a,b), we can identify the direct influence of many of the changes made in the PlioMIP2 mid-Pliocene boundary conditions (see also Figure S7 for a side-by-side comparison between the  $E^{280}$ ,  $E^{280,P}$ , and  $Eoi^{280}$  cases). The strongest temperature deviations are seen over parts of Antarctica and Greenland in the absence of land ice. Relatively cool temperatures in the  $Eoi^{400}$  can be found over  
 315 East Antarctica, where we have implemented a thicker ice sheet compared to the pre-industrial conditions. We see similar temperatures between the  $E^{280}$  and  $Eoi^{400}$  over much of the land at low latitudes, that are mainly a result of surface properties

in the Pliocene boundary conditions that counteract the overall warming (e.g. lakes in Africa, vegetation in Australia, see also supplementary Figure 1). Warmest month mean temperatures of  $>40^{\circ}\text{C}$  occur over many low and middle latitude continental regions, while coldest month mean temperature contours steadily migrate poleward in the Eoi<sup>400</sup>. As shown in Table 1, we see a considerable polar amplification in the overall warming pattern between the Eoi<sup>400</sup> and E<sup>280</sup> with mostly small temperature differences in the tropics increasing to  $>10^{\circ}\text{C}$  over both the Arctic and Southern Ocean.

Besides being warmer, the Eoi<sup>400</sup> is substantially wetter compared to the E<sup>280</sup> (Figure 4 c,d) with a global average annual precipitation of 1180mm versus 1042mm (i.e. a 13%; see Table 1). Polar regions are overall wetter, but most noticeably over the Southern Ocean. ~~This is in agreement with a larger ice volume over parts of East Antarctica~~ Reduced ice sheet cover over much of Antarctica and warmer surface temperatures both act to increase precipitation over much of the coastal region.

An overall poleward migration of storm tracks is seen, which is most pronounced over the North Atlantic Ocean. At lower latitudes, changes in the precipitation pattern are dominated by a shift towards the Eastern Hemisphere. Regions surrounding the Indian and West Pacific Ocean are much wetter in the Eoi<sup>400</sup> while those around the East Pacific and Atlantic Ocean become drier. This is related to a combined westward shift and expansion of the Walker circulation in our mid-Pliocene simulations (shown in most PlioMIP2 simulations by Han et al. 2021). Like many other comparable model studies (see e.g. Bellucci et al. 2010; Haywood et al. 2020), our E<sup>280</sup> shows a double inter-tropical convergence zone (ITCZ) over the Pacific Ocean (e.g. Bellucci et al. 2010; Haywood et al. 2020). The southern branch of the ITCZ is weaker over the Pacific Ocean in the Eoi<sup>400</sup>, while shifting westward and southward towards a pronounced South-Pacific Convergence Zone (SPCZ). A more active Indian Monsoon can explain increased rainfall over the Middle East and South Asia, as well as some of the cooler temperatures in northern India. Higher precipitation rates in the Eoi<sup>400</sup> are also seen over Australia and much of northern Africa, which are directly related to the altered land surface properties (see also Figure S1 in the supplementary material).

In addition to the direct effects of the PlioMIP2 boundary conditions, some more general changes in the atmospheric circulation are seen between the E<sup>280</sup> and Eoi<sup>400</sup> cases (Figure 4 e,f - note that the global average change in 500hPa height is subtracted in f). A reduction in the equator-to-pole gradient is not only present in surface temperatures, but also in mid-tropospheric height surfaces. This translates to an overall reduction of baroclinic instability, despite some of the increases in precipitation seen at middle and high latitudes. Reduced surface elevation over much of West Antarctica and Greenland leads to a lower surface pressure in the Eoi<sup>400</sup> while the opposite is seen over parts of East Antarctica. These changes in the surface topography also likely influence the circulation as several stationary ridges are evident in the 500hPa height difference. Preferred midlatitude ridging is evident over the North Pacific Ocean in the Eoi<sup>400</sup>, which is in turn reflected in the temperature and precipitation differences with the E<sup>280</sup>. In addition to the advective adjustment (i.e. warmer and wetter west of the high pressure/geopotential anomaly), the radiative feedback and subsidence act to also increase temperatures at towards the centre of the anomaly.

#### 4.2.2 Ocean

Annual mean sea surface temperatures (SSTs) reflect the patterns and changes seen in the Eoi<sup>400</sup> and E<sup>280</sup> atmospheric temperatures (Figure 5 a,b; a similar comparison using the E<sup>280,P</sup> instead can be found in supplementary Figure 8). In contrast to near surface air temperature, the Arctic Ocean SSTs show the smallest difference between the Eoi<sup>400</sup> and E<sup>280</sup> cases despite

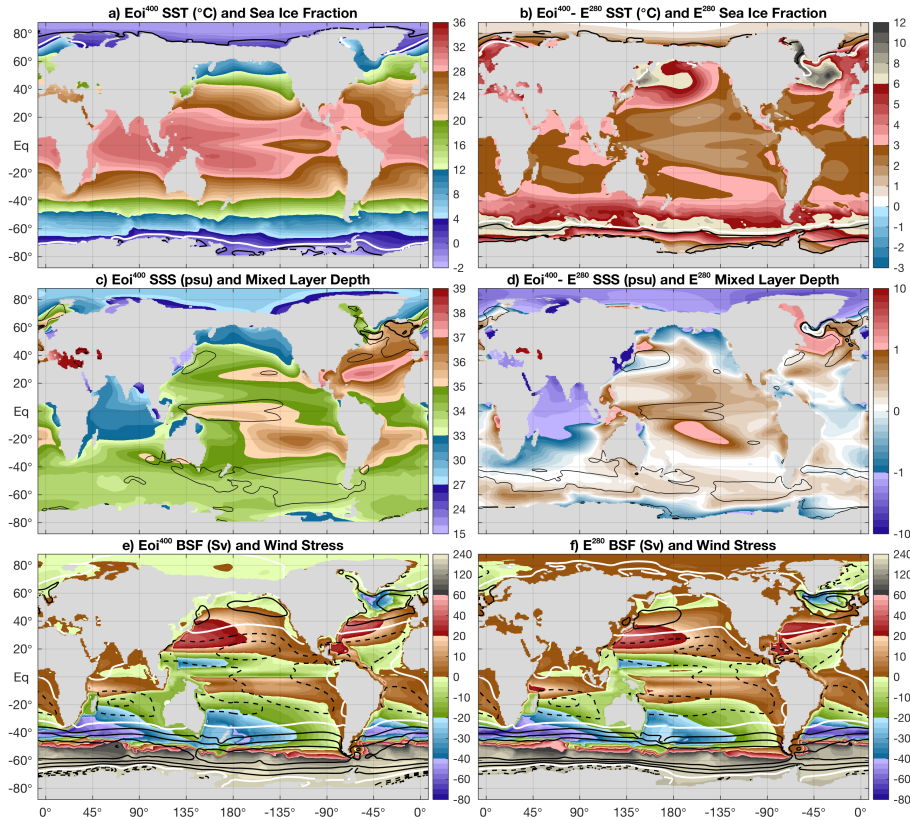


**Figure 5.** Annual mean oceanic observables-model fields from our  $Eoi^{400}$  case (left) and the  $Eoi^{400} - E^{280}$  difference. **a,b)** sea surface temperature temperature (shading) and sea ice fraction (contours; white: 0.15, eyan: 0.5, black: 0.5 and 0.9). Contours in (a):  $Eoi^{400}$ ; in (b)  $E^{280}$ . **c,d)** Sea surface salinity (shading) and mixed layer depth (thin line: 100m, thick black: 250m, thick white: 500m). **e,f)** Barotropic stream function (BSF; shading) and zonal wind stress (contours every  $5 \cdot 10^{-2}$  Pa, dashed:  $<0$ , thick white line at 0hPa). Contours in (e):  $Eoi^{400}$ ; in (f)  $E^{280}$ .

large reductions in sea ice cover. Another area with relatively cool temperatures in the Pliocene is the eastern Tropical Pacific Ocean, being still  $\sim 2^\circ\text{C}$  warmer compared to the  $E^{280}$ . Much warmer SSTs are seen over much of the North Atlantic Ocean, as well as the Northwest Pacific Ocean. Apart from the West Antarctic coastal region, the entire Southern Ocean is  $\sim 4-8^\circ\text{C}$  warmer in our Pliocene control.

- 355 Sea surface salinity (SSS) patterns in the  $Eoi^{400}$  are mostly driven by precipitation patterns and gateway changes (Figure, 5c,d) between the  $E^{280}$ . High precipitation amounts over most of Asia and the Indian Ocean cause low SSS through surface fluxes as well as river runoff. The Arctic Ocean is less saline compared to the  $E^{280}$  partly as a result of increased runoff, but also due to the closed Bering Strait and Northwest Passage. The outflow of these low salinity Arctic surface waters can be seen to the east and south of Greenland, resulting in a rather complex interaction with much more saline waters in the northern Atlantic Ocean.
- 360 The Pacific Ocean is in general more saline in the  $Eoi^{400}$ , with regional changes from the  $E^{280}$  that are the combined effect of

precipitation patterns, enhanced river runoff, and the Bering [Straight Strait](#) closure.

The depth averaged flow, represented by the barotropic stream function (BSF) in Figure 5 e,f is very similar between the  $E_{oi}^{400}$  and  $E^{280}$  cases. Regardless of the reduced meridional gradient in surface temperatures, the Antarctic Circumpolar Current (ACC) is slightly stronger in our Pliocene control. In contrast to what is seen at the surface, the depth-averaged density gradient is steeper in the  $E_{oi}^{400}$  and therefore enhances the density-driven component of the ACC. Southern Hemisphere subtropical gyres are slightly weaker, while those in the Northern Hemisphere show a poleward extension in the  $E_{oi}^{400}$ . North Atlantic subtropical and subpolar gyres are both stronger compared to the  $E^{280}$ .

### 4.2.3 Sea ice

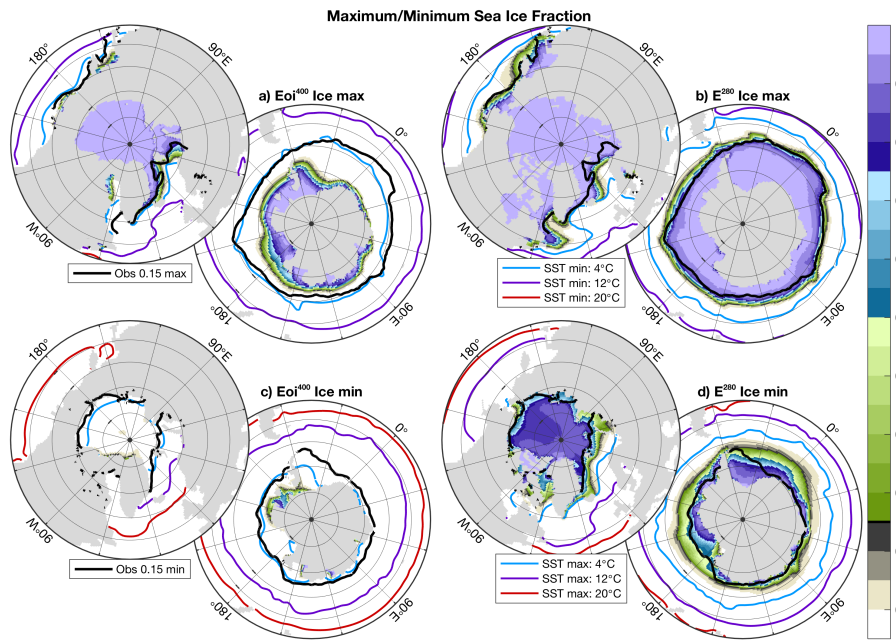


**Figure 6.** a)  $E^{280}$ - $E_{oi}^{400}$  mean maximum monthly sea ice fraction over northern and southern polar regions. Coloured contours show coldest month mean SST, the black contour indicates the late 21<sup>st</sup> century observed September (NH)/March (SH) sea ice edge at an 0.15 fraction (Fetterer et al., 2017) (indicated on the colour bar: Fetterer et al. 2017). b) As in (a), but for the  $E_{oi}^{400}$ - $E^{280}$  case using the same contour intervals and sea ice edge data. c-d) Similar to (a-b) showing the monthly sea ice minimum, warmest month mean SST and late 21<sup>st</sup> century observed March (NH)/September (SH) sea ice edge.

Even with the relatively simple model set-up used here, our  $E^{280}$  simulation has realistic sea ice cover compared to late 20<sup>th</sup> century observations from Peng et al. (2013) as shown in Figure 6. The mean sea ice maximum extent corresponds well with the observed modern day maximum in both hemispheres, but the minimum is overestimated especially in the Southern Hemisphere. The disagreement may, however, be mostly explained by the difference between pre-industrial and modern conditions. Sea ice cover is drastically reduced in our  $E_{oi}^{400}$  simulation compared to the  $E^{280}$  one. During the late summer minimum



extent, sea ice concentrations drop to nearly zero across both polar regions, with only some remaining over exposed waters in  
 375 West Antarctica. Changes in the maximum sea ice cover are less dramatic over the Arctic region, while the Southern Ocean  
 still has much less sea ice cover in the  $E_{oi}^{400}$  compared to the  $E^{280}$  case. This corresponds well with the  $\sim 4\text{--}8^\circ\text{C}$  warmer SSTs  
 seen across the Southern Ocean in our Pliocene simulations (Figure 5b). The isolated nature of the Arctic Ocean allows its  
 surface waters to remain relatively cool, with some sea ice persisting until late summer. Despite substantial refreezing during  
 wintertime, open waters in the early winter months prevent the air from cooling down further. This explains the much larger  
 380 near surface air temperature anomalies over the Arctic region between our  $E_{oi}^{400}$  and  $E^{280}$  simulations (Figure 4b).

### 4.3 Meridional overturning and heat transport

#### 4.3.1 Global

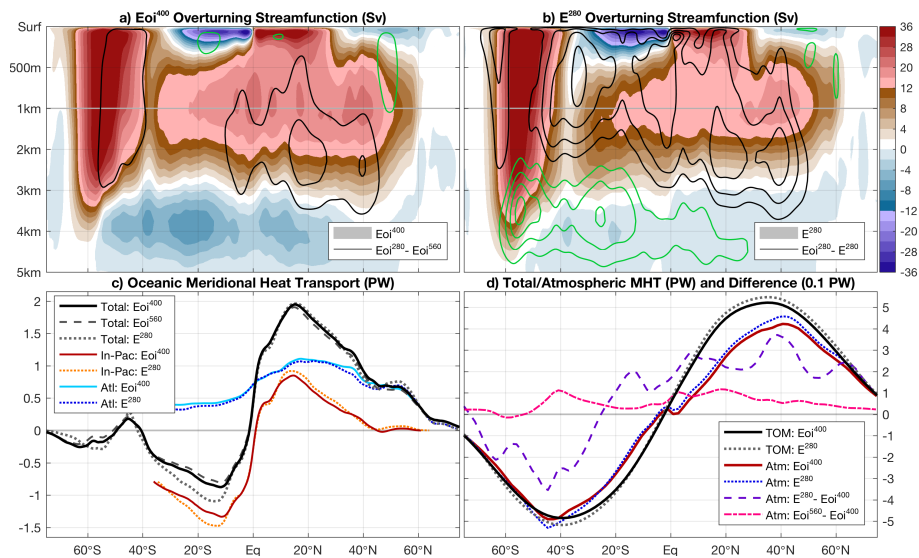


**Figure 7.** **a)** Global oceanic meridional overturning stream function (MSF) of the  $E_{oi}^{400}$  case (shading) and  $E_{oi}^{280} - E_{oi}^{560}$  difference (contours every 2Sv; black: positive and green: negative) simulations, taking the mean over the last 100–500 model years. **b)** As in (a), but for the  $E^{280}$  case and  $E_{oi}^{280}$  cases -  $E^{560}$  difference. Note the vertical stretching of the upper 1km; used contour intervals are highlighted in white on the colour bar. **c)** Oceanic meridional heat transport in the  $E_{oi}^{400}$  (solid lines; global: black, Indo-Pacific: red, and Atlantic Ocean: blue),  $E^{280}$  (dashed lines, similar colouring), and  $E_{oi}^{560}$  (dotted line, only global). **d)** Total meridional heat transport, induced by the top of model net radiative fluxes ( $E_{oi}^{400}$ : solid black,  $E^{280}$ : dotted grey) and the corresponding atmospheric heat transport (red) in the  $E_{oi}^{400}$ . Similar for the: solid red,  $E^{280}$  using grey and blue; dotted lines, respectively blue). The difference ( $\Delta$ ) in atmospheric heat transport with respect to the  $E_{oi}^{400}$  is shown for the  $E^{280}$  (dashed pink) and  $E_{oi}^{560}$  (dash-dotted pink), magnified tenfold.

Our  $E_{oi}^{400}$  case is characterised by a stronger and deeper global meridional overturning circulation (MOC) compared to the  $E^{280}$ . This is reflected in the global meridional overturning stream function (MSF) in Figure 7a,b by the dominant northern  
 385 overturning cell north of  $40^\circ\text{S}$ . The deep southern (i.e. negative) overturning cell linked to Antarctic bottom waters is slightly

stronger in the  $E_{oi}^{400}$  as well. Note that the appearance of this overturning cell is mostly masked in the Southern Ocean by strong Ekman upwelling linked to the ACC. The  $E_{oi}^{560}$  MOC is similar to the  $E_{oi}^{400}$  one, but overall slightly weaker, while the opposite holds for the  $E_{oi}^{280}$ . This can be partly a transient effect of the simulations, but suggests a tendency of the MOC to get weaker towards higher atmospheric  $pCO_2$ .

390 The differences in MSF pattern and strength between the  $E_{oi}^{400}$  and  $E^{280}$  cases are only partly reflected in the corresponding oceanic heat transports (OHT), shown in Figure 7c. Apart from a slight weakening of poleward heat transport at southern low latitudes (mostly in the Indo-Pacific sector), the  $E_{oi}^{400}$  OHT is very similar to the  $E^{280}$ . The warmer  $E_{oi}^{560}$  case has an overall reduced poleward oceanic heat transport, but the relative change is small ( $<0.1PW$ ). The total meridional heat transport (MHT, shown in Figure 7d), is slightly weaker in the  $E_{oi}^{400}$  compared to the  $E^{280}$ . This is a direct response the reduced meridional  
395 temperature gradient seen in the  $E_{oi}^{400}$ , demanding a lower poleward heat transport on both hemispheres. As there are only minor changes in the oceanic component, the reduced total MHT must be mainly accounted for by the atmosphere. This is clearly reflected ~~reflected by the~~ atmospheric MHT difference of  $E^{280}$  with respect to the  $E_{oi}^{400}$ , having mostly the same sign as the total MHT. The only exception is seen at southern low latitudes, where a stronger southward OHT is compensated by a northward atmospheric MHT in the  $E^{280}$ . The  $E_{oi}^{560}$  atmospheric MHT shows a small net positive offset with respect to  
400 the  $E_{oi}^{400}$ , that may be explained by some remnant warming trend. In agreement with a further reduction of the meridional temperature gradient, the warmer  $E_{oi}^{560}$  case thus has a further reduced poleward MHT albeit small ( $\sim 0.1 W m^{-2}$ ) and mostly accounted for by the ocean.

### 4.3.2 Atlantic Ocean

The Atlantic Meridional Overturning Circulation (AMOC; Figure 8a) clearly encompasses the entire deep northern overturning  
405 cell in the global MSF north of  $30^\circ S$  (Figure 7a). The AMOC mean state is overall stronger in our Pliocene versus pre-industrial simulations, but its temporal variability is also considerably higher in all of the Pliocene cases ( $22.7 \pm 1.6 Sv$  versus  $18.3 \pm 0.7 Sv$ ; see also Figure S5 in the supplementary material). Especially the  $E_{oi}^{560}$  AMOC undergoes a series of large ( $>10Sv$ ) intensity swings, although this is likely caused by the thermal adjustment of the deep ocean and therefore mostly a transient model feature. These large swings stopped after  $\sim 1000$  model years, but the AMOC variability remains the largest  
410 of any of our cases ( $\sigma = 2.4Sv$ ). The  $E^{280,P}$  AMOC also exhibits a larger variability ( $\sigma = 1.0Sv$ ) compared to the other pre-industrial cases, but still smaller than any of the Pliocene ones. A more detailed discussion on AMOC variability is provided in Section 4.6.2

The difference in AMOC streamfunction between  $E_{oi}^{400}$  and  $E^{280}$  is most pronounced between 1 and 3 km depth (Figure 8b). The stronger and deeper AMOC cell can be partly explained by the altered vertical mixing parameters in our Pliocene model  
415 set-up, as the  $E^{280,P}$  shows a reduced but very similar difference pattern with respect to the  $E_{oi}^{400}$ . This is consistent with the stronger AMOC in the *POPI* type vertical mixing simulations of Chandan and Richard Peltier (2017). In general, we find that the altered vertical mixing scheme in our Pliocene simulations does have an impact on the strength and behaviour of the AMOC, but not to the extent that is seen in any of the Pliocene cases. It is therefore likely that the altered boundary conditions and resulting circulation changes have a considerable impact on the AMOC strength and behaviour. ~~The applied~~ A stronger

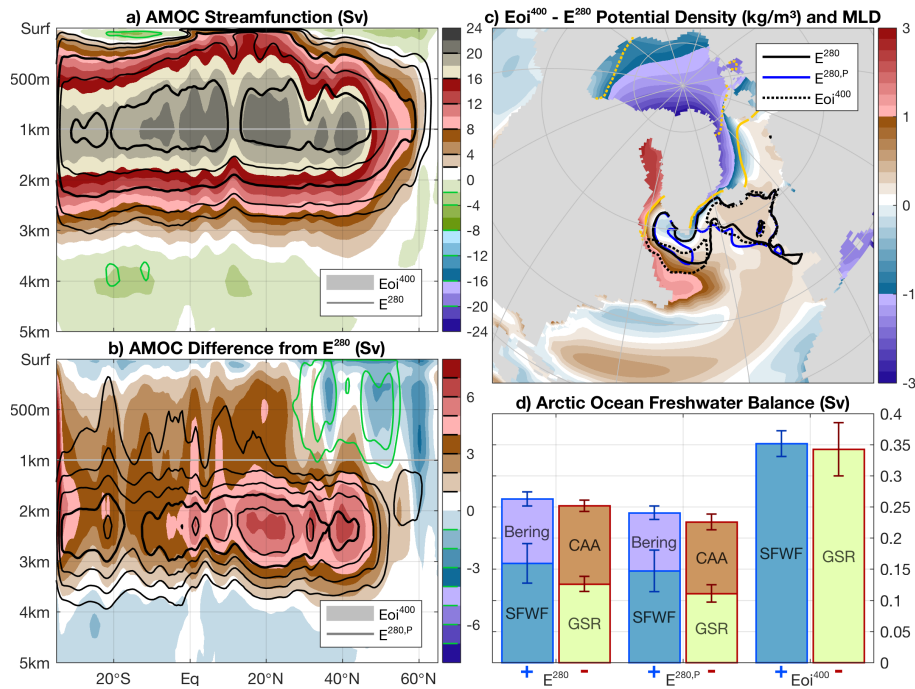


**Figure 8.** a) Mean AMOC stream function over the last 500 years of the  $Eoi^{400}$  (shading) and  $E^{280}$  simulation (contours,  $-$  highlighted on the [colour bar](#)). b) Difference in AMOC stream function with respect to the  $E^{280}$ , for the  $Eoi^{400}$  (shading) and the  $E^{280,P}$  (contours). c)  $Eoi^{400} - E^{280}$  (100-year mean) potential density difference, averaged over the upper 100m and relative to the global average change. Contours show the annual mean maximum mixed layer depth for the  $E^{280}$  (solid black),  $E^{280,P}$  (solid blue), and  $Eoi^{400}$  (dotted black) [and 0.15 sea ice fraction \(yellow; solid:  \$E^{280}\$  dashed:  \$Eoi^{400}\$ \)](#). d) Freshwater budget over the Arctic Ocean for the (left to right)  $E^{280}$ ,  $E^{280,P}$ , and  $Eoi^{400}$  cases, including the net surface freshwater flux (SFWF) and transports across the Bering Strait, Canadian Archipelago (CAA), and Greenland-Scotland Ridge (GSR). The mean over the last 500 model years is taken, with the standard deviation of yearly averages indicated by the error bars.

420 [mid-Pliocene AMOC was found consistently in the PlioMIP2 ensemble by Zhang et al. \(2021\), who also found a link with higher North Atlantic SSTs, but no clear relation with Atlantic OHT. The latter is investigated in more detail by Weifenbach et al. \(in prep\), who decompose the OHT into the contributions from the overturning and gyre circulations, respectively. The PlioMIP2 boundary conditions \[applied here\]\(#\) include the closure of several high latitude oceanic gateways. This results in lighter upper ocean waters across the Arctic Ocean in the  \$Eoi^{400}\$ , but denser waters across most of the North Atlantic Ocean \(Figure](#)

425 [8c\)](#). The integrated net surface freshwater flux over the Arctic Ocean more than doubles in the  $Eoi^{400}$  case compared to the  $E^{280}$  one (Figure 8d). This more than compensates for the missing transport from the Bering straight closure. Lacking connectivity through the Canadian Archipelago demands for an equally large net southward freshwater transport across the Greenland-Scotland ridge. The outflow of those light, low salinity Arctic waters pushes the deep water formation zone towards the south across the Labrador Sea into warmer and deeper waters. Increased salinity in the Labrador Sea and thus higher potential

430 densities are tied to the closure of the Canadian Archipelago, as shown by the negative component in the  $E^{280}$  Arctic Ocean freshwater balance (i.e. net salt transport from Labrador Sea). Such a southward shift of the deep water formation zone is not present in the  $E^{280,P}$  case.

#### 4.4 Model-proxy comparison

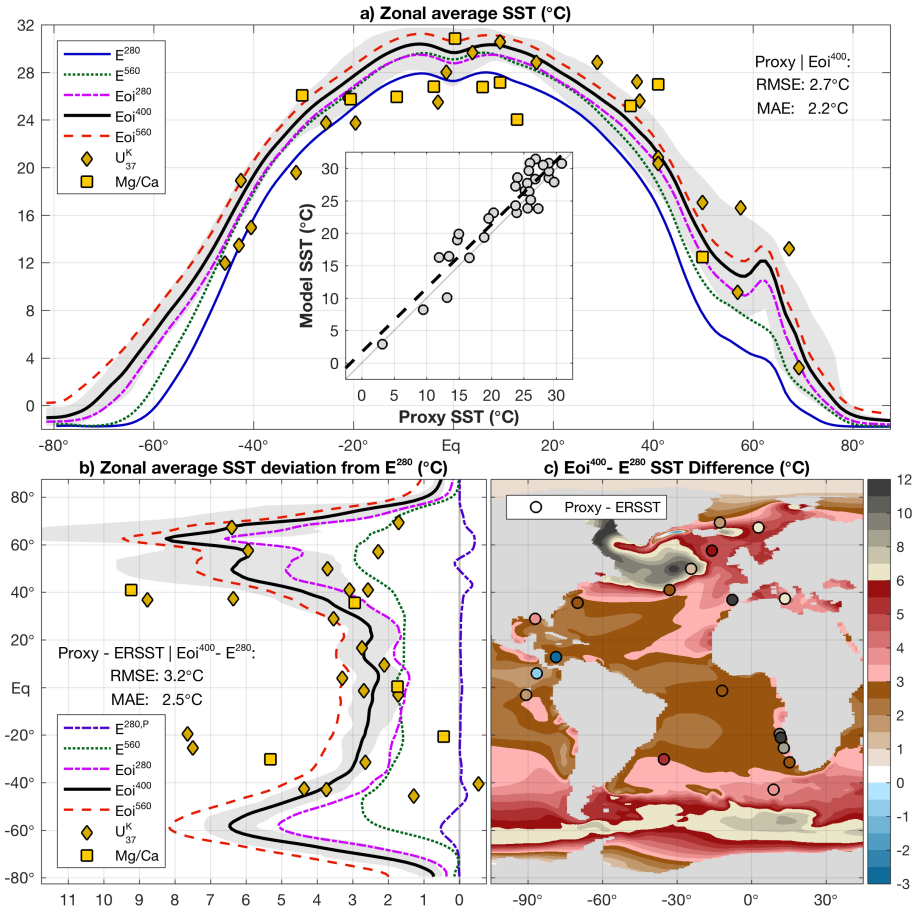


**Figure 9.** a) PRISM4-proxy-based Proxy-based annual mean SST reconstructions (yellow markers; diamonds:  $U_{37}^K$ , squares: Mg/Ca) versus model-derived zonally averaged SST for  $Eoi^{400}$  (black, including zonal variation in grey),  $E^{280}$  (blue),  $E^{560}$  (green dotted),  $Eoi^{280}$  (pink dash-dotted), and  $Eoi^{560}$  (orange dashed). The inset shows a point-wise comparison, including a simple linear regression. b) Pliocene proxy - pre-industrial SST (ERSST; late 19<sup>th</sup> century reanalysis) and modelled zonal average SST difference from  $E^{280}$  (colouring as in a; purple dash-dotted:  $E^{280,P}$ ). c) Pliocene - pre-industrial SST difference over the Atlantic Ocean: proxy - PI-reanalysis-pre-industrial (coloured markers) and model-derived  $Eoi^{400} - E^{280}$  (shading).

As shown by Haywood et al. (2020), our  $Eoi^{400}$  case performs well when comparing the annual mean SSTs to the available PlioMIP2 time-specific proxy records (Foley and Dowsett, 2019)(Foley and Dowsett, 2019; McClymont et al., 2020). The

zonally averaged, annual mean SST from our different simulations is shown in light of these proxies in Figure 9a. Considering site-specific rather than zonally averaged SSTs from the Eoi<sup>400</sup> simulations, we find a root mean square error (RMSE) of ~~3.52~~2.7°C and a mean absolute error (MAE) of ~~2.52~~2.2°C (using the combined U<sub>37</sub><sup>K'</sup> and Mg/Ca proxy record of McClymont et al. 2020). Moreover, there is no significant warm or cold model bias across the SST/latitude range covered by the proxies. Relatively  
440 warm North Atlantic SSTs in the model are well reflected by the proxy record, ~~apart from a single site in the high-latitude North Atlantic (ODP site 909) where our Eoi<sup>400</sup> case is showing a ~15°C lower SST consistent with the other CCSM/CESM models within PlioMIP2 as shown by de Nooijer et al. (2020). They also find that the CCSM/CESM model family best captures mid-Pliocene Arctic SST proxies, which is likely related to low sea ice cover.~~

Looking at the SST difference between Pliocene and pre-industrial conditions, rather than absolute values, reveals some more  
445 discrepancies between proxy records and our Eoi<sup>400</sup> simulation (Figure 9b). Most of the high positive temperature anomalies at northern middle and high latitudes remain well captured by the model, as well as the much smaller differences at low latitudes. However, other sites at both northern and southern middle latitudes show a much poorer agreement between model-based and proxy indicated Pliocene - pre-industrial SST differences. The lack of proxy data across most of the Southern Ocean makes it impossible to assess whether the large SST differences between our Pliocene and pre-industrial simulations are realistic. De-  
450 spite the ~~seemingly poor visual~~visually poor agreement compared to absolute ~~Pliocene SSTs, mid-Pliocene SSTs, the~~ RMSE and MAE ~~indices~~ are only slightly ~~lower~~higher for the Pliocene - pre-industrial SST difference.

Surprisingly large Pliocene - pre-industrial SST differences (considering a limited CO<sub>2</sub> effect) were found in the PlioMIP1, especially over the North Atlantic Ocean, but not well reflected in the model ensemble (Haywood et al., 2013b). This seems to be greatly improved now, as shown by the large positive anomalies over much of the middle to high latitude North Atlantic  
455 Ocean in Figure 9c. The largest discrepancies between proxy-based and model-derived Pliocene - pre-industrial SST differences are seen in the Mediterranean Sea and off the coasts of northern America and southern Africa. These discrepancies can be largely explained by coastal upwelling and boundary currents, which are poorly resolved in our simulations because of the limited horizontal resolution (e.g. ~~McClymont et al. 2020~~McClymont et al. 2020; Li et al. 2019). Although absolute Pliocene SSTs seem to agree better, they are already much too warm at some of these locations in our E<sup>280</sup> case compared to reanalysis  
460 data.

Near surface air temperatures reveal the same warming pattern between the Eoi<sup>400</sup> and E<sup>280</sup> case as seen in the SSTs over low and middle latitudes (see also Figure S9 in the supplementary material). The highest temperature anomalies shift poleward, over the Arctic Ocean and the Antarctic coastal region due to sea ice melt and reduced ice sheet cover. ~~It is noteworthy that even our~~Our coolest Pliocene simulation (Eoi<sup>280</sup>) is similar or even warmer than the E<sup>560</sup> case at all latitudes. This indicates  
465 the importance of the implemented mid-Pliocene model boundary conditions and long-term impacts such as the partial loss of ice sheets.

#### 4.5 Sensitivity to Pliocene boundary conditions versus atmospheric pCO<sub>2</sub>

Using our set of pre-industrial and Pliocene *sensitivity* simulations (i.e. E<sup>280</sup>, E<sup>560</sup>, Eoi<sup>280</sup>, and Eoi<sup>560</sup>), we can make an assessment of the effects of the applied Pliocene boundary conditions (Eoi<sup>n</sup>- E<sup>n</sup>) versus external radiative forcing (X<sup>560</sup>- X<sup>280</sup>), as well

470 as any state-dependency in the model response. The difference in annual mean near surface air temperature is shown in Figure 10. The top panels of this figure show the modelled temperature response to a shift from pre-industrial to Pliocene boundary conditions (excluding CO<sub>2</sub>), the bottom ones to a doubling atmospheric pCO<sub>2</sub>. Consequently, comparing left to right panels shows the state-dependency of the effect of boundary conditions to a different pCO<sub>2</sub> baseline (top), and vice versa (bottom). Some generic temperature differences between the model cases can be easily identified in all of these comparisons. Stronger  
475 contrasts are seen over land than over the ocean, as a result of the thermal capacity and much larger potential for latent heat fluxes over the ocean. Polar amplification of the temperature change also seems universal across our simulations, caused mainly by ice-albedo feedbacks and reversed lapse rate feedbacks (i.e. positive at high latitudes, negative at low latitudes; [see also Figure S7 in the supplementary material](#)). As noted before, the ECS of our simulated Pliocene climate is very similar to that of the pre-industrial one (i.e. 3.2°C versus 3.17°C per CO<sub>2</sub> doubling). It is therefore not surprising that the overall response  
480 to a doubling of atmospheric pCO<sub>2</sub> is comparable, with mainly some regional differences as a result of the boundary conditions and local feedback mechanisms.

~~A similar comparison of atmospheric temperatures between our~~ [Changes in precipitation patterns between the four sensitivity cases is made in Figure S7 in the supplementary material, showing the zonally averaged vertical distribution. The combination of surface albedo and lapse rates causes low latitude regions to warm mostly in](#) [simulations show large differences between the response to atmospheric pCO<sub>2</sub> and other model boundary conditions. In line with the findings of Han et al. \(2021\), the effect of a CO<sub>2</sub> doubling is mainly a wet gets wetter/dry gets drier-response and focusses in the upper troposphere, while high latitude regions do so near the surface. This general response is again seen in all of the four comparisons made between the tropics. Differences in precipitation between Pliocene and pre-industrial cases are generally much more pronounced and widespread, but are also enhanced between the high versus low CO<sub>2</sub> scenarios. Some of these differences are directly related to the boundary conditions \(mainly topography and ice sheets\) and their temperature response \(e.g. sea ice, monsoons\). In addition, large-scale precipitation changes include a westward and poleward shift in the tropics resulting in a wetter tropical Indian and West Pacific Ocean in our mid-Pliocene simulations. Han et al. \(2021\) show that these dynamic changes in precipitation are related to the meridional and zonal circulation patterns \(e.g. Walker Circulation influences the Indian-Pacific moisture exchange\). Moreover, our CCSM4-Utr simulations are found to exhibit the largest asymmetry in hemispheric energy flux within the PlioMIP2 ensemble, explaining the significant shifts of the Pacific ITCZ and SPCZ. Further north, we see a poleward migration of North Atlantic storm tracks and the dynamic response of a prevailing North Pacific anticyclone. These shifts in precipitation correspond well with what is seen in Figure 4d.](#)

485  
490  
495

[We also consider the zonally averaged temperature differences between the four sensitivity cases, with along with the corresponding energy balance model \(EBM\) analysis and the contribution from its different components \(Figure 11\). All of the zonally averaged temperature responses estimated using the EBM are in near perfect agreement with the actual surface temperature differences in the model. Simply adding the contributions from albedo, emissivity and MHT reproduces the full temperature response well, showing that nonlinear effects between them are small. Both these findings are in line with the results of Hill et al. \(2014\) for PlioMIP1. Albedo plays a crucial role in the response to mid-Pliocene boundary conditions, especially](#)

500

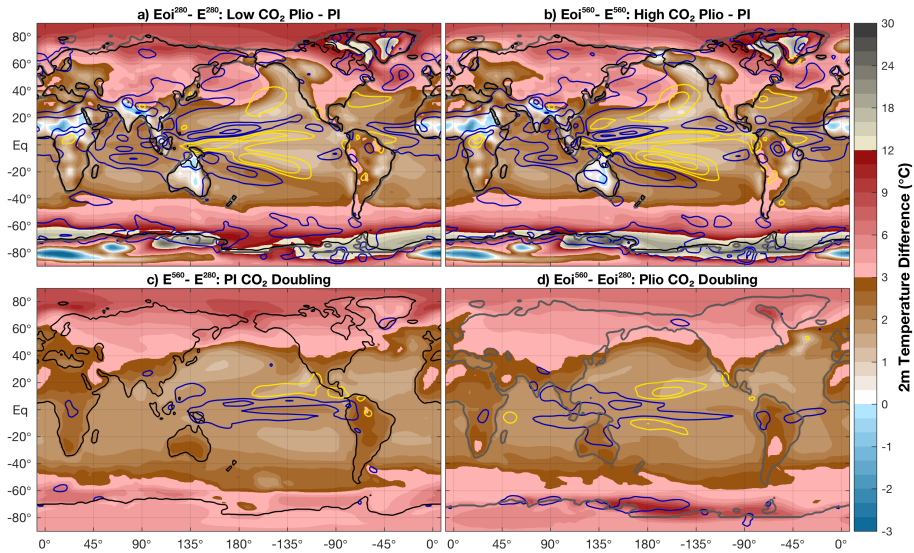


**Figure 10.** Annual mean near surface air temperature difference between our four *sensitivity* simulations; **a)**  $E_{oi}^{280} - E^{280}$ : Low  $CO_2$  Plio - PI **b)**  $E_{oi}^{560} - E^{560}$ : High  $CO_2$  Plio - PI **c)**  $E^{560} - E^{280}$  and **d)**  $E_{oi}^{560} - E_{oi}^{280}$ : PI  $CO_2$  Doubling. Contours showing the difference in mean annual precipitation at 100, 200 and 500 mm; blue: positive and yellow: negative.

505 at the surface (i.e. vegetation, ice sheets, and sea ice). The effect of planetary albedo is about a third lower compared to the surface, showing that the latter is partly compensated by the shortwave contribution from clouds, aerosols and water vapour. The emissivity of longwave radiation shows a more similar response between the effect of boundary conditions vs.  $CO_2$  doubling, but is still stronger in the former. About half of the temperature contribution through emissivity after a  $CO_2$  doubling is related to the direct radiative forcing, leaving the other half as mainly the result of water vapour and lapse rate

510 feedbacks. These feedbacks, together with the surface albedo, are thus the main drivers behind polar amplification of the temperature difference between all of the different cases considered here. The effect is partly mitigated by meridional heat transport and cloud feedbacks, but these have little impact on the global scale. This is again consistent with the findings of Hill et al. (2014), with a larger effect of the exception of stronger high latitude warming near the surface after introducing Pliocene boundary conditions and stratospheric cooling in response to higher  $pCO_2$ . We also observe a more negative lapse rate

515 feedback in the warmer Pliocene cases, mostly at low and middle latitudes, likely as a result of higher SSTs and atmospheric moisture mid-Pliocene boundary conditions in PlioMIP2 versus PlioMIP1.

Most of the effects of the Pliocene model boundary conditions on temperature (Figure 10 a,b) agree well with those seen earlier between our  $E^{280}$  and  $E_{oi}^{400}$  cases, shown in Figure 4b. The warming effect of removing/lowering ice sheets at high latitudes and cooling effect of introducing lakes or removing desert at low latitudes are independent of the atmospheric  $CO_2$  level.

520 Over the Arctic Ocean, reduced sea ice in the Pliocene simulations has an increased impact on temperatures above the surface towards lower  $pCO_2$  (Figure 10 a vs. b). The opposite is seen over parts of the Southern Ocean, where sea ice cover is still

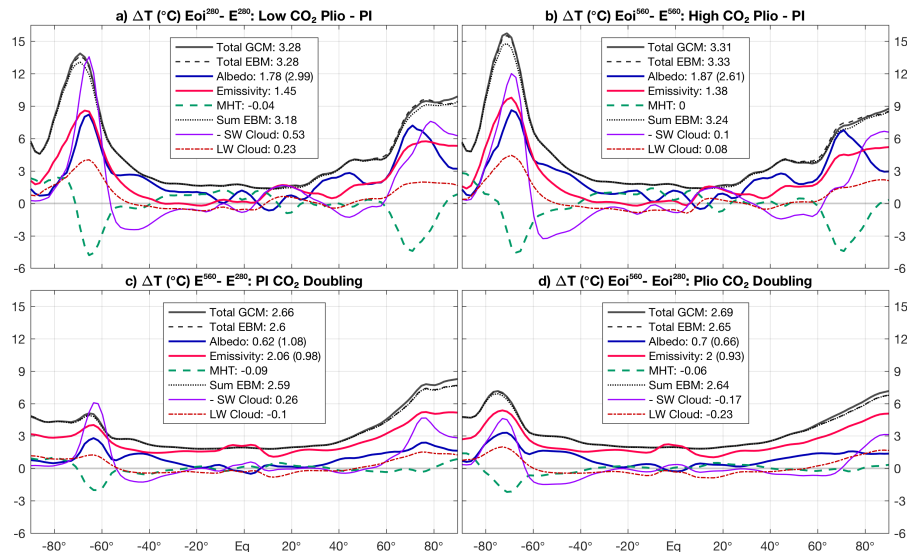


**Figure 11.** Annual mean near-surface air  $\Delta T$  as in Figure 10, but showing zonally averaged temperature differences and contributions from different components within the energy balance model (EBM). The temperature difference between our four sensitivity simulations (Total GCM; **a**)  $E_{oi}^{280} - E^{280}$  (solid gray) is compared to the one predicted by the EBM (Total EBM; dashed dark grey). Components of the EBM include: planetary albedo (solid blue), **b**)  $E_{oi}^{560} - E^{560}$  emissivity (solid red), **c**)  $E^{560} - E^{280}$  meridional heat transport (MHT; dashed green), shortwave cloud forcing (negative; solid purple) and **d**)  $E_{oi}^{560} - E_{oi}^{280}$  longwave (dashed dark red) cloud forcing. The sum of the contributions from albedo, emissivity and MHT is also shown (Sum EBM; dashed black). Globally averaged values are shown for each component, with bracketed values added for surface albedo and emissivity excluding the effect of CO<sub>2</sub> doubling.

relatively large in the  $E^{560}$  (see also contours in Figure ?? Figure S10 in the supplementary material). Temperature changes that can be related to altered circulation patterns in the Pliocene versus pre-industrial (e.g. monsoons, South Pacific Convergence Zone, midlatitude ridging, storm tracks) are robust between different CO<sub>2</sub> levels. The temperature response to a doubling of atmospheric pCO<sub>2</sub> is very similar at low and middle latitudes between our pre-industrial and Pliocene simulations (Figure 10 c,d). Differences in sea ice cover (and to a lesser extent land ice and surface properties) amplify high latitude warming in response to a CO<sub>2</sub> doubling, most prominently over the Arctic in the pre-industrial cases and over the Southern Ocean in the Pliocene ones.

As in figure 10, but for sea surface temperature (SST), showing also the annual mean sea ice edge (i.e. 0.15 ice fraction) in black contours; solid:  $E^{280}$ , dashed:  $E^{560}$ , dotted:  $E_{oi}^{280}$ , and dash-dotted:  $E_{oi}^{560}$  (only 2 shown per panel). The near surface air temperature differences between our four sensitivity cases (Figure 10) are reflected in the SST, as shown in Figure ?? (see Figure S10 in the supplementary material). The most prominent exception to this consistency is found over high latitude surface waters, which are seen to change much less in temperature than the air above. Moreover, any comparison showing a relatively large difference in near-surface air temperature has a reduced SST difference over the same high latitude waters (e.g. Figures 10 and ??; a,c vs. b,d for the Arctic Ocean). This can be explained by the decoupling effect of sea ice, which tends to dampen



the SST differences. Contour lines in Figure ?? indeed suggest a large reduction in sea ice cover over the Southern Ocean for Eoi<sup>560</sup> (but with large seasonal differences). Pliocene - Eoi<sup>280</sup>, while little change is seen for E<sup>560</sup> - E<sup>280</sup>. Also over the Arctic Ocean, the dampening effect of sea ice on SST differences is stronger for cooler reference states (Figure ?? a,c vs. b,d). The annual mean sea ice edge at northern high latitudes shows limited changes between the simulations, as the effect is highly seasonal (strong reductions in summer, see also Figure 6). The SST difference pre-industrial SST differences over the Pacific Ocean between Pliocene and pre-industrial cases is are consistent between CO<sub>2</sub> levels and noticeably different from the effect of a pCO<sub>2</sub> doubling. These patterns suggest a shift in the background state of both ENSO and PDO in our Pliocene simulations (see also Section 4.6). An even more prominent and consistent SST response to the Pliocene boundary conditions is found over the North Atlantic Ocean (also seen in Figure 5b). This is likely the combined result of a stronger Pliocene AMOC and the isolation of the Labrador Sea through closure of the Canadian Archipelago. Large changes in SST between our Pliocene and pre-industrial simulations are also seen in the Southern Ocean. These can be linked to the upwelling of relatively warm deep waters south of the ACC. In contrast to the dampening effect of sea ice, the effect of upwelling near the ACC is the same at or above the ocean surface, and reflected in the air temperatures above (Figure 10).

## 550 4.6 Modes of internal variability

### 4.6.1 El Niño Southern Oscillation

Not only the mean state, but several modes of variability in our simulated Pliocene climate are also different from what is seen in the pre-industrial reference. As it plays a primary role in the tropics, we first look at the behaviour of the El Niño Southern Oscillation (ENSO). In Figure 12, time series of the Niño 1+2 and Niño 3.4 indices are shown for the E<sup>280</sup> and Eoi<sup>400</sup> case. The amplitude of both ENSO indices is greatly reduced in our Eoi<sup>400</sup> versus E<sup>280</sup> case ( $\sigma_{1+2}$ : -54%;  $\sigma_{3.4}$ : -68%). This is the largest such reduction seen among the PlioMIP2 ensemble, as shown by Oldeman et al. (2021) (Figure 2a of Oldeman et al. 2021; OB21). Furthermore, the occurrence of strong and long-lasting (>1°C; >1 year) El Niño/La Niña events completely disappears in our mid-Pliocene simulation. Both these findings are consistent among all of our mid-Pliocene (i.e. Eoi<sup>280</sup>, Eoi<sup>400</sup>, Eoi<sup>560</sup>) versus pre-industrial (i.e. E<sup>280</sup>, E<sup>280,P</sup>, E<sup>560</sup>, E<sup>1120</sup>) cases (not shown).

560 Spectral analysis of the Niño 3.4 indices also shows large differences between the ENSO behaviour in the E<sup>280</sup> and Eoi<sup>400</sup> case. The modelled pre-industrial ENSO variability is characterised by a broad spectral peak at periods of 3–10 years, with 3 statistically significant (at 99% confidence) peaks and a dominant period around 6 years. A similar broad peak is seen for the mid-Pliocene ENSO, but only with significant variability at 4 years (99%) and 9 years (95%). Moreover, there is a lot more an increase of significant variability in the Eoi<sup>400</sup> case at shorter periods around 2 years or less. This agrees well with the predominantly weak and rather high frequent behaviour of the modelled Pliocene ENSO, seen in the Niño 3.4 time series. A similar drop in spectral power of the mid-Pliocene ENSO is seen consistently in the PlioMIP2 ensemble, but more focussed at the 3–5 year period (Figures 3 and 4 of OB21).

As to be expected from both of the Niño time series shown for each case, the amplitude of SST anomalies is seen to be much smaller throughout the tropical Pacific Ocean in our Eoi<sup>400</sup> versus E<sup>280</sup> case. Looking at the mean SST pattern corresponding

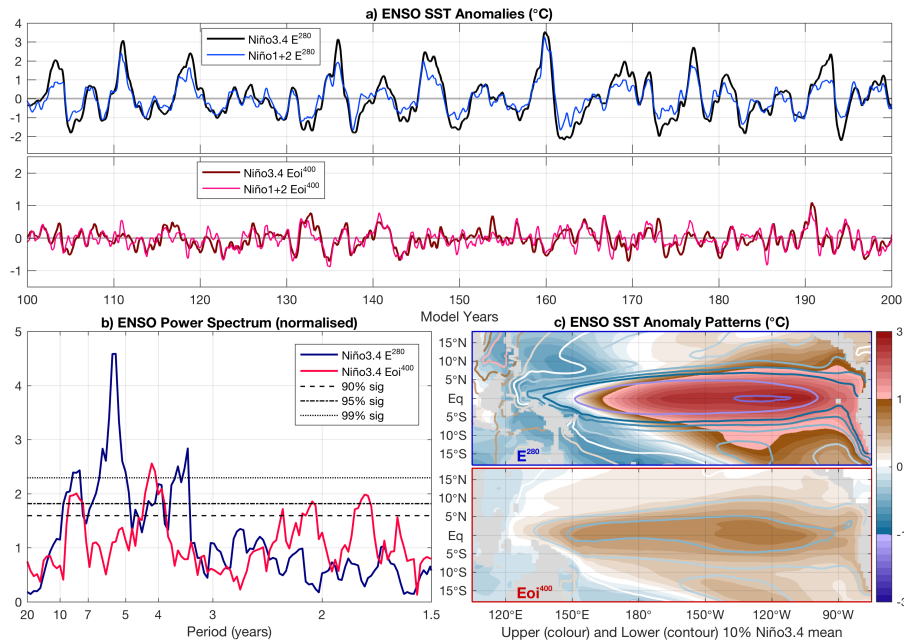


**Figure 12.** **a)** ENSO time series for the  $E^{280}$  (blue) and  $Eoi^{400}$  (red), using monthly SST anomaly fields and a 5-month running mean. Note the different scaling; temperature intervals are kept the same for visual comparison. **b)** Multi-taper power spectrum, using 200 years of monthly data including 90%, 95% and 99% confidence levels based. **c)** Corresponding ENSO SST patterns, taking the mean over the 10% highest (shading) and 10% lowest (contours) monthly Niño 3.4 index values at each location.

570 to the 10% average highest and lowest monthly Niño 3.4 values allows us to assess both the spatial distribution and strength of ENSO variability at the same time. In addition to an overall highly reduced amplitude, the associated region of SST variability expands westward and poleward across the Central/West Pacific Ocean in our Pliocene simulation. [This is consistent with the pattern shifts shown by the majority PlioMIP2 models \(Figure 5 of OB21\).](#) The mean difference in SST between the  $Eoi^{400}$  and  $E^{280}$  (Figure 5b) over the main region of ENSO variability is smaller than the average tropics. The background state of the tropical Pacific Ocean is therefore not El Niño-, but rather slightly La Niña-like. [Only few models within the PlioMIP2 ensemble show such a strong La Niña-like pattern in the mean temperature of the  \$Eoi^{400}\$ , but these are also the models with the largest reduction in ENSO variability](#) (see also [Oldeman et al. 2021 Figures 9-11 of OB21](#)).

575

#### 4.6.2 Interannual to multi-decadal SST variability

Using 500 years of annual mean SSTs and AMOC strength, we assess the dominant modes of variability in the North Pacific and North Atlantic Ocean (Figure 13). We consider the dominant eigenmode of SST anomalies in the North Pacific Ocean to represent the PMV, and the one best correlating with average North Atlantic SSTs as the AMV. The explained variance by the PMV mode is seen to decrease in the  $Eoi^{400}$  versus  $E^{280}$  case, while that of the AMV greatly increases. As noted earlier, the AMOC variability is considerably larger in the  $Eoi^{400}$  case compared to the  $E^{280}$  one. Correlations between the PMV, AMV,

580

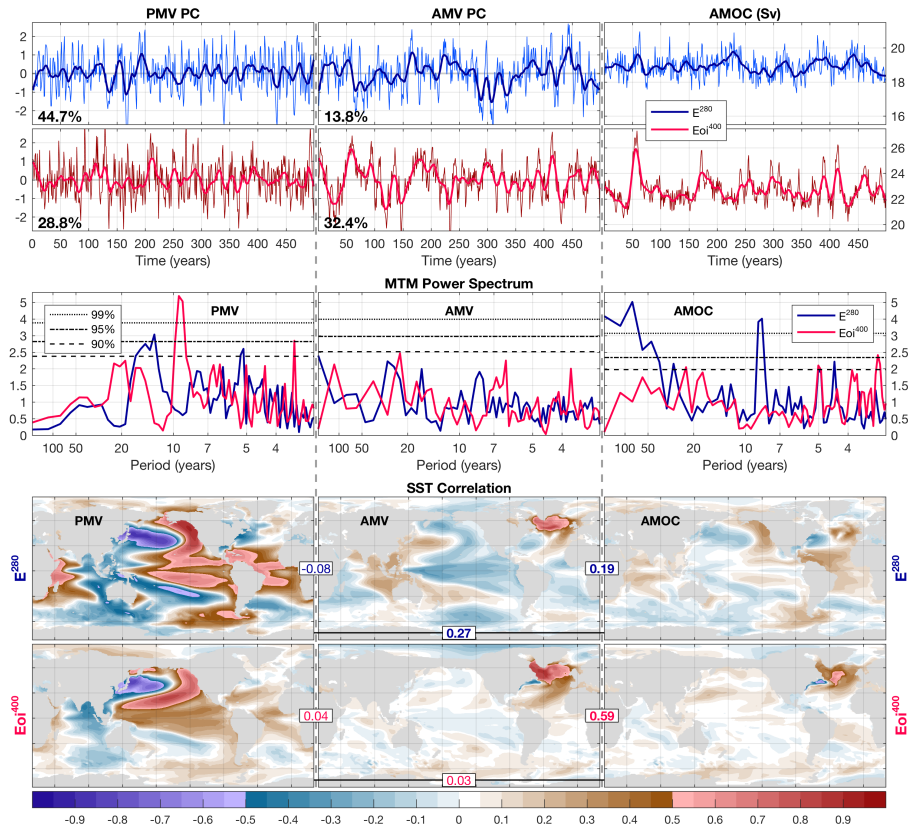


**Figure 13.** Time series (upper panels; thick lines using a 20-year smoothing window), multi-tapered power spectra (middle panels), and spatial correlation patterns (lower panels) of North Pacific SST (left), North Atlantic SST (middle), and AMOC strength (right) variability, for 500 years of annual SST data from our  $E^{280}$  (blue) and  $Eoi^{400}$  (red) simulation. The percentage of variance explained by the respective principal component is shown in black along with the PMV and AMV time series. Spatial SST patterns show the temporal correlation between the SST at each location and the different variability indices. Boxed numbers also indicate the total correlation between each of these indices (i.e. time series in the upper panels.)

AMOC and annual Niño 3.4 indices can be found in Figure S11-S12 in the supplementary material.

585 Spectral analysis shows that the  $E^{280}$  PMV has a broad peak at 10–20 years and therefore strongly resembles the Pacific Decadal Oscillation (PDO). This broad peak is seen to shift towards longer periods for the  $Eoi^{400}$  PMV, which is now accompanied by a sharper peak at just under 10 years. Looking at the patterns of SST variability associated to the PMV, an almost global footprint in the  $E^{280}$  is reduced to mostly a North Pacific signature in the  $Eoi^{400}$ . This is likely related to the strongly decreased ENSO variability in the  $Eoi^{400}$  versus  $E^{280}$  case, as both the low latitude SST patterns and the spectral properties at periods <10 years

590 show a high resemblance between PMV and ENSO in both simulations. This is supported by significant correlations ( $E^{280}$ : 0.48;  $Eoi^{400}$ : 0.34) between the PMV and yearly Niño 3.4 indices. The role of the AMV on global SST variability is much more limited compared to PMV, but again strongest and more widespread in the  $E^{280}$  case. Meanwhile, the  $Eoi^{400}$  has a much

higher percentage of explained variance and is strongly connected to AMOC variability. The spatial pattern of SST anomalies associated to the AMOC strength shows little resemblance to either the PMV or AMV in the E<sup>280</sup> case, but both their time series are significantly (yet weakly) correlated. In contrast, the AMOC strength strongly correlates with the AMV for the Eoi<sup>400</sup> and their associated spatial patterns show a large resemblance. It is thus clear that the stronger and more variable AMOC in our Pliocene simulations has a profound impact on not only the mean North Atlantic SSTs, but also their variability. Additionally, it seems that the different modes of SST variability are less connected between ocean basins in the Eoi<sup>400</sup> versus E<sup>280</sup> case.

## 5 Conclusions

We have completed a set of simulations using the CCSM4/CESM1.0.5 within the PlioMIP2, including E<sup>280</sup>, E<sup>560</sup>, Eoi<sup>280</sup>, Eoi<sup>400</sup>, and Eoi<sup>560</sup> cases (E<sup>280,P</sup> and E<sup>1120</sup> as additional sensitivity experiments). Our simulations show a warm mPWP climate, which is 4.7°C warmer compared to our pre-industrial control in terms of globally averaged near surface air temperature. With an estimated ECS of 3.1°C per CO<sub>2</sub> doubling, which is consistent throughout the different pre-industrial and Pliocene cases, much of the mPWP signal is thus related to the effect of the applied PRISM4 boundary conditions. The effect of those boundary conditions is mainly to increase temperatures by about 3°C on average globally and 2.4°C in the ocean. The vertical distribution of oceanic temperatures is altered in our Pliocene simulations by the use of enhanced background vertical diffusivity. ~~The additional Our E<sup>280,P</sup> experiment shows that this differential warming patterns can be fully explained by the effect of this different parameter choice between the simulation can explain most of this differential warming pattern between pre-industrial and Pliocene experiments. None of the cases. The enhanced vertical mixing acts to warm the deep ocean at the expense of the upper ocean, without affecting the globally averaged surface temperature. Most of the other results are thus not significantly influenced by the altered vertical diffusivity, with only minor regional differences seen at the surface and throughout the that become negligible throughout the rest of the atmosphere.~~

The combined effect of increased atmospheric pCO<sub>2</sub> and altered boundary conditions not only make our Eoi<sup>400</sup> case warmer than the E<sup>280</sup> one, but also induce substantial polar amplification. This is mainly the result of ~~surface albedo feedbacks, reduced ice sheet cover and latitudinally dependent latitudinally dependent surface albedo (ice and vegetation), water vapour and lapse rate feedbacks. Cloud feedbacks are small in the global average, with the shortwave component acting to mitigate high latitude warmth.~~ The temperature differences are most pronounced where ice sheets are removed (including a ~~strong large~~ elevation effect) and high latitude oceans, where sea ice cover is greatly reduced in all of the Pliocene cases. ~~Especially the shortwave radiative feedbacks resulting from the mid-Pliocene boundary conditions are much stronger compared to those from a CO<sub>2</sub> doubling. Furthermore, the latitudinal dependence in all of the considered radiative components is stronger, helping to explain the relatively warm high latitude regions in our Pliocene simulations.~~ The Eoi<sup>400</sup> climate shows an increased precipitation rate with respect to the E<sup>280</sup> one. Both equatorial and high latitude regions are generally wetter in the Pliocene, while the sub-tropics become ~~dryer drier~~ (with a distinct poleward shift of the storm tracks). Particularly high precipitation amounts are seen over most of the Indian Ocean and its surroundings, owing to enhanced North African and South/Southeast Asian monsoons in the

Pliocene.

The warmer Eoi<sup>400</sup> climate with a reduced meridional temperature gradient compared to the pre-industrial reference agrees well with the available proxies. A strong Pliocene warming signal over the North Atlantic Ocean is seen in both the proxy record and our simulations, which can be linked to an enhanced AMOC. This stronger AMOC, however, is not linked to an overall  
630 increase in oceanic meridional heat transport. Moreover, the total (atmosphere + ocean) top of model induced meridional heat transport is slightly reduced in the warmer simulations, in line with the reduced meridional temperature gradient. The stronger and more variable AMOC in our Pliocene versus pre-industrial simulations can in part be explained by the altered vertical diffusivity parameter. Yet, it is mostly the result of the applied mid-Pliocene boundary conditions, in particular the closure of several Arctic gateways.

635

In addition to differences in the mean state between our Eoi<sup>400</sup> and E<sup>280</sup> cases, there are clear shifts in the different modes of variability studied here: ENSO, PMV and AMV. The ENSO amplitude is greatly reduced in our Pliocene simulations and characterised by shorter periodicity compared to the pre-industrial reference. The corresponding spatial pattern is also spread out across much of the tropical Pacific Ocean. Closely related to ENSO is the PMV in our E<sup>280</sup> case, both having a distinct  
640 fingerprint on global SST variability on various time scales ranging from annual to multi-decadal. This teleconnection is lost in the Eoi<sup>400</sup> case, with the PMV influence being mostly confined to just the North Pacific Ocean. Meanwhile, the AMV shows a strong connection to AMOC variability in our Pliocene simulations. Their mutual influence seems to be the dominant source of SST variability in the Eoi<sup>400</sup>, as opposed to ENSO/PMV in the E<sup>280</sup>.

As most of the PRISM4 boundary conditions, which are applied here as an external forcing to the model simulation, are in fact  
645 the result of long term feedbacks (i.e. ice melt and vegetation changes), the Eoi<sup>400</sup> can serve as a good analog for future climatic changes. Our simulations show not only a strong warming compared to the pre-industrial reference, but also considerable regional changes and shifts in the dominant modes of variability.

*Data availability.* PlioMIP2 model data, including those of the simulations presented here, can be downloaded from the server located at the School of Earth and Environment of the University of Leeds. Contact Alan Haywood (a.m.haywood@leeds.ac.uk) for access. The  
650 last 100 model years of our E<sup>280</sup>, E<sup>560</sup>, Eoi<sup>280</sup>, Eoi<sup>400</sup>, and Eoi<sup>560</sup> are available within the dataset. PlioMIP2 data from CESM2, EC-Earth3.3, NorESM1-F, IPSLCM6A and GISS2.1G can be obtained through the Earth System Grid Federation (ESGF) (<https://esgf-node.llnl.gov/search/cmip6/>, last access: 14 October 2021, ESGF, 2021).

*Author contributions.* MAK, MLJB, and ASvdH set up the model simulations, MAK and MLJB managed the simulations and post-processing of the data. MLJB performed the analyses and set up the manuscript. All authors contributed to the final shape and contents of the manuscript.

655 *Competing interests.* The authors declare to have no competing interests.

*Acknowledgements.* This work was carried out under the program of the Netherlands Earth System Science Centre (NESSC), financially supported by the Ministry of Education, Culture and Science (OCW, grant #024.002.001). Simulations were performed at the SURFsara dutch national computing facilities and were sponsored by NWO-EW (Netherlands Organisation for Scientific Research, Exact Sciences) under the projects 17189 and 2020.022.

660 **References**

- Baatsen, M., von der Heydt, A. S., Huber, M., Kliphuis, M. A., Bijl, P. K., Sluijs, A., and Dijkstra, H. A.: The middle to late Eocene greenhouse climate modelled using the CESM 1.0.5, *Climate of the Past*, 16, 2573–2597, <https://doi.org/10.5194/cp-16-2573-2020>, 2020.
- Bellucci, A., Gualdi, S., and Navarra, A.: The double-ITCZ syndrome in coupled general circulation models: The role of large-scale vertical circulation regimes, *Journal of Climate*, 23, 1127–1145, <https://doi.org/10.1175/2009JCLI3002.1>, 2010.
- 665 Bitz, C. M., Shell, K. M., Gent, P. R., Bailey, D. A., Danabasoglu, G., Armour, K. C., Holland, M. M., and Kiehl, J. T.: Climate sensitivity of the community climate system model, version 4, *Journal of Climate*, 25, 3053–3070, <https://doi.org/10.1175/JCLI-D-11-00290.1>, 2012.
- Blackmon, M., Boville, B., Bryan, F., Dickinson, R., Gent, P., Kiehl, J., Moritz, R., Randall, D., Shukla, J., Solomon, S., Bonan, G., Doney, S., Fung, I., Hack, J., Hunke, E., Hurrell, J., Kutzbach, J., Meehl, J., Otto-Bliesner, B., Saravanan, R., Schneider, E. K., Sloan, L., Spall, M., Taylor, K., Tribbia, J., and Washington, W.: The Community Climate System Model, *Bulletin of the American Meteorological Society*, 670 82, 2357–2376, [https://doi.org/10.1175/1520-0477\(2001\)082<2357:TCCSM>2.3.CO;2](https://doi.org/10.1175/1520-0477(2001)082<2357:TCCSM>2.3.CO;2), 2001.
- Bloch-Johnson, J., Pierrehumbert, R. T., and Abbot, D. S.: Feedback temperature dependence determines the risk of high warming, *Geophysical Research Letters*, 42, 4973–4980, <https://doi.org/10.1002/2015GL064240>, 2015.
- Burke, K. D., Williams, J. W., Chandler, M. A., Haywood, A. M., Lunt, D. J., and Otto-Bliesner, B. L.: Pliocene and Eocene provide best analogs for near-future climates, *Proceedings of the National Academy of Sciences of the United States of America*, 115, 13 288–13 293, 675 <https://doi.org/10.1073/pnas.1809600115>, 2018.
- Caballero, R. and Huber, M.: State-dependent climate sensitivity in past warm climates and its implications for future climate projections, *Proceedings of the National Academy of Sciences*, 110, 14 162–14 167, <https://doi.org/10.1073/pnas.1303365110>, <http://www.pnas.org/cgi/doi/10.1073/pnas.1303365110>, 2013.
- Chandan, D. and Richard Peltier, W.: Regional and global climate for the mid-Pliocene using the University of Toronto version of CCSM4 and PlioMIP2 boundary conditions, *Climate of the Past*, 13, 919–942, <https://doi.org/10.5194/cp-13-919-2017>, 2017.
- 680 Danabasoglu, G., Ferrari, R., and McWilliams, J. C.: Sensitivity of an ocean general circulation model to a parameterization of near-surface eddy fluxes, *Journal of Climate*, 21, 1192–1208, <https://doi.org/10.1175/2007JCLI1508.1>, 2008.
- Danabasoglu, G., Bates, S. C., Briegleb, B. P., Jayne, S. R., Jochum, M., Large, W. G., Peacock, S., and Yeager, S. G.: The CCSM4 ocean component, *Journal of Climate*, 25, 1361–1389, <https://doi.org/10.1175/JCLI-D-11-00091.1>, 2012.
- 685 de Nooijer, W., Zhang, Q., Li, Q., Zhang, Q., Li, X., Zhang, Z., Guo, C., Nisancioglu, K. H., Haywood, A. M., Tindall, J. C., Hunter, S. J., Dowsett, H. J., Stepanek, C., Lohmann, G., Otto-Bliesner, B. L., Feng, R., Sohl, L. E., Chandler, M. A., Tan, N., Contoux, C., Ramstein, G., Baatsen, M. L., Von Der Heydt, A. S., Chandan, D., Peltier, W. R., Abe-Ouchi, A., Chan, W. L., Kamae, Y., and Brierley, C. M.: Evaluation of Arctic warming in mid-Pliocene climate simulations, *Climate of the Past*, 16, 2325–2341, <https://doi.org/10.5194/cp-16-2325-2020>, 2020.
- 690 Deser, C., Phillips, A. S., Tomas, R. A., Okumura, Y. M., Alexander, M. A., Capotondi, A., Scott, J. D., Kwon, Y. O., and Ohba, M.: ENSO and pacific decadal variability in the community climate system model version 4, *Journal of Climate*, 25, 2622–2651, <https://doi.org/10.1175/JCLI-D-11-00301.1>, 2012.
- Dowsett, H., Robinson, M., Haywood, A., Salzmann, U., Hill, D., Sohl, L., Chandler, M., Williams, M., Foley, K., and Stoll, D.: The PRISM3D paeoenvironmental reconstruction, *Micropaleontology Press*, 2010.

- 695 Dowsett, H., Dolan, A., Rowley, D., Moucha, R., Forte, A. M., Mitrovica, J. X., Pound, M., Salzmann, U., Robinson, M., Chandler, M.,  
Foley, K., and Haywood, A.: The PRISM4 (mid-Piacenzian) paleoenvironmental reconstruction, *Climate of the Past*, 12, 1519–1538,  
<https://doi.org/10.5194/cp-12-1519-2016>, 2016.
- Etminan, M., Myhre, G., Highwood, E. J., and Shine, K. P.: Radiative forcing of carbon dioxide, methane, and nitrous oxide: A signifi-  
cant revision of the methane radiative forcing, *Geophysical Research Letters*, 43, 12,614–12,623, <https://doi.org/10.1002/2016GL071930>,  
700 2016.
- Farnsworth, A., Lunt, D. J., Brien, C. L. O., and Foster, G. L.: Climate Sensitivity on Geological Timescales Controlled by Nonlinear  
Feedbacks and Ocean Circulation, *Geophysical Research Letters*, pp. 9880–9889, <https://doi.org/10.1029/2019GL083574>, <https://doi.org/10.1029/2019GL083574>, 2019.
- Fetterer, F., Knowles, K., Meier, W., Savaoie, M., and Windnagel, K.: Sea ice index, version 3, <https://doi.org/10.7265/N5K072F8>, 2017.
- 705 Foley, K. and Dowsett, H.: Community sourced mid-Piacenzian sea surface temperature (SST) data: U.S. Geological Survey data release,  
<https://doi.org/10.5066/P9YP3DTV>, 2019.
- Gent, P. R. and McWilliams, J. C.: Isopycnal Mixing in Ocean Circulation Models, [https://doi.org/10.1175/1520-0485\(1990\)020<0150:IMIOCM>2.0.CO;2](https://doi.org/10.1175/1520-0485(1990)020<0150:IMIOCM>2.0.CO;2), 1990.
- Gent, P. R., Danabasoglu, G., Donner, L. J., Holland, M. M., Hunke, E. C., Jayne, S. R., Lawrence, D. M., Neale, R. B., Rasch, P. J.,  
710 Vertenstein, M., Worley, P. H., Yang, Z. L., and Zhang, M.: The community climate system model version 4, *Journal of Climate*, 24,  
4973–4991, <https://doi.org/10.1175/2011JCLI4083.1>, 2011.
- Ghil, M., Allen, M. R., Dettinger, M. D., Ide, K., Kondrashov, D., Mann, M. E., Robertson, A. W., Saunders, A., Tian, Y., Varadi, F., and Yiou,  
P.: Advanced spectral methods for climatic time series, *Reviews of Geophysics*, 40, 3–1–3–41, <https://doi.org/10.1029/2000RG000092>,  
2002.
- 715 Gregory, J. M., Ingram, W. J., Palmer, M. A., Jones, G. S., Stott, P. A., Thorpe, R. B., Lowe, J. A., Johns, T. C., and  
Williams, K. D.: A new method for diagnosing radiative forcing and climate sensitivity, *Geophysical Research Letters*, 31, 2–5,  
<https://doi.org/10.1029/2003GL018747>, 2004.
- Han, Z., Zhang, Q., Li, Q., Feng, R., Haywood, A., Tindall, J., Hunter, S., Otto-Bliesner, B., Brady, E., Rosenbloom, N., Zhang, Z., Li, X.,  
Guo, C., Nisancioglu, K., Stepanek, C., Lohmann, G., Sohl, L., Chandler, M., Tan, N., Ramstein, G., Baatsen, M., Heydt, A., Chandan,  
720 D., Peltier, W. R., Williams, C., Lunt, D., Cheng, J., Wen, Q., and Burls, N.: Evaluating the large-scale hydrological cycle response within  
the PlioMIP2 ensemble, *Climate of The Past Discussions*, pp. 1–32, <https://doi.org/10.5194/cp-2021-72>, 2021.
- Haywood, A. M., Dolan, A. M., Pickering, S. J., Dowsett, H. J., McClymont, E. L., Prescott, C. L., Salzmann, U., Hill, D. J., Hunter,  
S. J., Lunt, D. J., Pope, J. O., and Valdes, P. J.: On the identification of a pliocene time slice for data-model comparison, *Philosophical  
Transactions of the Royal Society A: Mathematical, Physical and Engineering Sciences*, 371, <https://doi.org/10.1098/rsta.2012.0515>,  
725 2013a.
- Haywood, A. M., Hill, D. J., Dolan, A. M., Otto-Bliesner, B. L., Bragg, F., Chan, W. L., Chandler, M. A., Contoux, C., Dowsett, H. J., Jost, A.,  
Kamae, Y., Lohmann, G., Lunt, D. J., Abe-Ouchi, A., Pickering, S. J., Ramstein, G., Rosenbloom, N. A., Salzmann, U., Sohl, L., Stepanek,  
C., Ueda, H., Yan, Q., and Zhang, Z.: Large-scale features of Pliocene climate: Results from the Pliocene Model Intercomparison Project,  
*Climate of the Past*, 9, 191–209, <https://doi.org/10.5194/cp-9-191-2013>, 2013b.
- 730 Haywood, A. M., Dowsett, H. J., Dolan, A. M., Rowley, D., Abe-Ouchi, A., Otto-Bliesner, B., Chandler, M. A., Hunter, S. J., Lunt, D. J.,  
Pound, M., and Salzmann, U.: The Pliocene Model Intercomparison Project (PlioMIP) Phase 2: Scientific objectives and experimental  
design, *Climate of the Past*, 12, 663–675, <https://doi.org/10.5194/cp-12-663-2016>, 2016.



- Haywood, A. M., Tindall, J. C., Dowsett, H. J., Dolan, A. M., Foley, K. M., Hunter, S. J., Hill, D. J., Chan, W. L., Abe-Ouchi, A., Stepanek, C., Lohmann, G., Chandan, D., Peltier, R. W., Tan, N., Contoux, C., Ramstein, G., Li, X., Zhang, Z., Guo, C., Nisancioglu, K. H., Zhang, Q., Li, Q., Kamae, Y., Chandler, M. A., Sohl, L. E., Otto-Bliesner, B. L., Feng, R., Brady, E. C., von der Heydt, A. S., Baatsen, M. L., and Lunt, D. J.: The Pliocene Model Intercomparison Project Phase 2: Large-scale climate features and climate sensitivity, *Climate of the Past*, 16, 2095–2123, <https://doi.org/10.5194/cp-16-2095-2020>, 2020.
- Heinemann, M., Jungclaus, J. H., and Marotzke, J.: Warm Paleocene/Eocene climate as simulated in ECHAM5/MPI-OM, *Clim. Past*, 5, 785–802, <https://doi.org/10.5194/cp-5-785-2009>, [www.clim-past.net/5/785/2009/](http://www.clim-past.net/5/785/2009/), 2009.
- Herold, N., Buzan, J., Seton, M., Goldner, A., Green, J. a. M., Müller, R. D., Markwick, P., and Huber, M.: A suite of Early Eocene (~55 Ma) climate model boundary conditions, *Geoscientific Model Development*, 7, 2077–2090, <https://doi.org/10.5194/gmd-7-2077-2014>, [www.geosci-model-dev.net/7/2077/2014/](http://www.geosci-model-dev.net/7/2077/2014/), 2014.
- Hill, D. J., Haywood, A. M., Lunt, D. J., Hunter, S. J., Bragg, F. J., Contoux, C., Stepanek, C., Sohl, L., Rosenbloom, N. A., Chan, W. L., Kamae, Y., Zhang, Z., Abe-Ouchi, A., Chandler, M. A., Jost, A., Lohmann, G., Otto-Bliesner, B. L., Ramstein, G., and Ueda, H.: Evaluating the dominant components of warming in Pliocene climate simulations, *Climate of the Past*, 10, 79–90, <https://doi.org/10.5194/cp-10-79-2014>, 2014.
- Huang, B., Thorne, P. W., Banzon, V. F., Boyer, T., Chepurin, G., Lawrimore, J. H., Menne, M. J., Smith, T. M., Vose, R. S., and Zhang, H. M.: Extended reconstructed Sea surface temperature, Version 5 (ERSSTv5): Upgrades, validations, and intercomparisons, *Journal of Climate*, 30, 8179–8205, <https://doi.org/10.1175/JCLI-D-16-0836.1>, 2017.
- Hunke, E. C. and Lipscomb, W. H.: The Los Alamos sea ice model, documentation and software., Tech. Rep. LA-CC-06-012, version 4., 2008.
- Hurrell, J. W., Holland, M. M., Gent, P. R., Ghan, S., Kay, J. E., Kushner, P. J., Lamarque, J. F., Large, W. G., Lawrence, D., Lindsay, K., Lipscomb, W. H., Long, M. C., Mahowald, N., Marsh, D. R., Neale, R. B., Rasch, P., Vavrus, S., Vertenstein, M., Bader, D., Collins, W. D., Hack, J. J., Kiehl, J., and Marshall, S.: The community earth system model: A framework for collaborative research, *Bulletin of the American Meteorological Society*, 94, 1339–1360, <https://doi.org/10.1175/BAMS-D-12-00121.1>, 2013.
- Kiehl, J. T., Shields, C. A., Hack, J. J., and Collins, W. D.: The climate sensitivity of the Community Climate System Model version 3 (CCSM3), *Journal of Climate*, 19, 2584–2596, <https://doi.org/10.1175/JCLI3747.1>, <https://journals.ametsoc.org/doi/full/10.1175/JCLI3747.1>, 2006.
- Knutti, R. and Rugenstein, M. A.: Feedbacks, climate sensitivity and the limits of linear models, *Philosophical Transactions of the Royal Society A: Mathematical, Physical and Engineering Sciences*, 373, <https://doi.org/10.1098/rsta.2015.0146>, 2015.
- Large, W. G., McWilliams, J. C., and Doney, S. C.: Oceanic Vertical Mixing - a Review and a Model with a Nonlocal Boundary-Layer Parameterization, *Reviews of Geophysics*, 32, 363–403, <https://doi.org/10.1029/94rg01872>, 1994.
- Lawrence, D. M., Oleson, K. W., Flanner, M. G., Thornton, P. E., Swenson, S. C., Lawrence, P. J., Zeng, X., Yang, Z.-L., Levis, S., Sakaguchi, K., Bonan, G. B., and Slater, A. G.: Parameterization improvements and functional and structural advances in Version 4 of the Community Land Model, *Journal of Advances in Modeling Earth Systems*, 3, <https://doi.org/10.1029/2011MS00045>, <http://doi.wiley.com/10.1029/2011MS00045>, 2011.
- Li, Z., Luo, Y., Arnold, N., and Tziperman, E.: Reductions in Strong Upwelling-Favorable Wind Events in the Pliocene, *Paleoceanography and Paleoclimatology*, 34, 1931–1944, <https://doi.org/10.1029/2019PA003760>, 2019.
- Loptson, C. A., Lunt, D. J., and Francis, J. E.: Investigating vegetation-climate feedbacks during the early Eocene, *Climate of the Past*, 10, 419–436, <https://doi.org/10.5194/cp-10-419-2014>, 2014.

- Lunt, D. J., Bragg, F., Chan, W. L., Hutchinson, D. K., Ladant, J. B., Morozova, P., Niezgodzki, I., Steinig, S., Zhang, Z., Zhu, J., Abe-Ouchi, A., Anagnostou, E., De Boer, A. M., Coxall, H. K., Donnadiou, Y., Foster, G., Inglis, G. N., Knorr, G., Langebroek, P. M., Lear, C. H., Lohmann, G., Poulsen, C. J., Sepulchre, P., Tierney, J. E., Valdes, P. J., Volodin, E. M., Dunkley Jones, T., Hollis, C. J., Huber, M., and Otto-Bliesner, B. L.: DeepMIP: Model intercomparison of early Eocene climatic optimum (EECO) large-scale climate features and comparison with proxy data, *Climate of the Past*, 17, 203–227, <https://doi.org/10.5194/cp-17-203-2021>, 2021.
- 775 McClymont, E. L., Ford, H. L., Ling Ho, S., Tindall, J. C., Haywood, A. M., Alonso-Garcia, M., Bailey, I., Berke, M. A., Littler, K., Patterson, M. O., Petrick, B., Peterse, F., Christina Ravelo, A., Risebrobakken, B., De Schepper, S., Swann, G. E., Thirumalai, K., Tierney, J. E., van der Weijst, C., White, S., Abe-Ouchi, A., Baatsen, M. L., Brady, E. C., Chan, W. L., Chandan, D., Feng, R., Guo, C., von der Heydt, A. S., Hunter, S., Li, X., Lohmann, G., Nisancioglu, K. H., Otto-Bliesner, B. L., Peltier, R. W., Stepanek, C., and Zhang, Z.: Lessons from a high-CO<sub>2</sub> world: An ocean view from ~3 million years ago, *Climate of the Past*, 16, 1599–1615, <https://doi.org/10.5194/cp-16-1599-2020>, 2020.
- 780 Neale, R. B., Richter, J., Park, S., Lauritzen, P. H., Vavrus, S. J., Rasch, P. J., and Zhang, M.: The Mean Climate of the Community Atmosphere Model (CAM4) in Forced SST and Fully Coupled Experiments, *Journal of Climate*, 26, 5150–5168, <https://doi.org/10.1175/JCLI-D-12-00236.1>, 2013.
- 785 Oldeman, A. M., Baatsen, M. L. J., von der Heydt, A. S., Dijkstra, H. A., Tindall, J. C., Abe-Ouchi, A., Booth, A. R., Brady, E. C., Chan, W.-L., Chandan, D., Chandler, M. A., Contoux, C., Feng, R., Guo, C., Haywood, A. M., Hunter, S. J., Kamae, Y., Li, Q., Li, X., Lohmann, G., Lunt, D. J., Nisancioglu, K. H., Otto-Bliesner, B. L., Peltier, W. R., Pontes, G. M., Ramstein, G., Sohl, L. E., Stepanek, C., Tan, N., Zhang, Q., Zhang, Z., Wainer, I., and Williams, C. J. R.: Reduced El Niño variability in the mid-Pliocene according to the PlioMIP2 ensemble, *Climate of the Past*, 17, 2427–2450, <https://doi.org/10.5194/cp-17-2427-2021>, 2021.
- 790 Oleson, K. W., Lawrence, D. M., Gordon, B., Flanner, M. G., Kluzek, E., Peter, J., Levis, S., Swenson, S. C., Thornton, E., Dai, A., Decker, M., Dickinson, R., Feddema, J., Heald, C. L., Lamarque, J.-f., Niu, G.-y., Qian, T., Running, S., Sakaguchi, K., Slater, A., Stöckli, R., Wang, A., Yang, L., Zeng, X., and Zeng, X.: Technical Description of version 4.0 of the Community Land Model ( CLM ), NCAR Tech. Note, NCAR/TN-47, 2010.
- Peng, G., Meier, W. N., Scott, D. J., and Savoie, M. H.: A long-term and reproducible passive microwave sea ice concentration data record for climate studies and monitoring, *Earth System Science Data*, 5, 311–318, <https://doi.org/10.5194/essd-5-311-2013>, 2013.
- 795 Rosenbloom, N. A., Otto-Bliesner, B. L., Brady, E. C., and Lawrence, P. J.: Simulating the mid-Pliocene Warm Period with the CCSM4 model, *Geoscientific Model Development*, 6, 549–561, <https://doi.org/10.5194/gmd-6-549-2013>, <http://www.geosci-model-dev.net/6/549/2013/>, 2013.
- Smith, R. D. and McWilliams, J. C.: Anisotropic horizontal viscosity for ocean models, *Ocean Modelling*, 5, 129–156, [https://doi.org/10.1016/S1463-5003\(02\)00016-1](https://doi.org/10.1016/S1463-5003(02)00016-1), 2003.
- 800 Smith, R. D., Jones, P., Briegleb, B., Bryan, F., Danabasoglu, G., Dennis, J., Dukowicz, J., Eden, C., Fox-Kemper, B., Gent, P., Hecht, M., Jayne, S., Jochum, M., Large, W., Lindsay, K., Maltrud, M., Norton, N., Peacock, S., Vertenstein, M., and Yeager, S.: The Parallel Ocean Program (POP) reference manual: Ocean component of the Community Climate System Model (CCSM), Los Alamos National Laboratory Tech. Rep. LAUR-10-01853, 141, 1–141, [www.cesm.ucar.edu/models/cesm1.0/pop2/doc/sci/POPRefManual.pdf](http://www.cesm.ucar.edu/models/cesm1.0/pop2/doc/sci/POPRefManual.pdf), 2010.
- 805 Steele, M., Morley, R., and Ermold, W.: PHC: A global ocean hydrography with a high-quality Arctic Ocean, *Journal of Climate*, 14, 2079–2087, [https://doi.org/10.1175/1520-0442\(2001\)014<2079:PAGOHW>2.0.CO;2](https://doi.org/10.1175/1520-0442(2001)014<2079:PAGOHW>2.0.CO;2), 2001.
- Trenberth, K. E. and Shea, D. J.: Atlantic hurricanes and natural variability in 2005, *Geophysical Research Letters*, 33, 1–4, <https://doi.org/10.1029/2006GL026894>, 2006.

Zhang, Z., Li, X., Guo, C., Helge Otterä, O., Nisancioglu, K. H., Tan, N., Contoux, C., Ramstein, G., Feng, R., Otto-Bliesner, B. L., Brady,  
810 E., Chandan, D., Richard Peltier, W., Baatsen, M. L., Von Der Heydt, A. S., Weiffenbach, J. E., Stepanek, C., Lohmann, G., Zhang,  
Q., Li, Q., Chandler, M. A., Sohl, L. E., Haywood, A. M., Hunter, S. J., Tindall, J. C., Williams, C., Lunt, D. J., Chan, W. L., and  
Abe-Ouchi, A.: Mid-Pliocene Atlantic Meridional Overturning Circulation simulated in PlioMIP2, *Climate of the Past*, 17, 529–543,  
<https://doi.org/10.5194/cp-17-529-2021>, 2021.

## Supplementary Tables and Figures

**Table S1.** Implemented fraction of CLM4 plant functional types (PFTs; see below) for each of the given PRISM4 megabiomes.

Megabiome	#	0	1	2	3	4	5	6	7	8	9	10	11	12	13	14
Tropical forest	1					0.75		0.25								
Warm-temperate forest	2		0.34				0.33		0.33							
Savannah and dry woodland	3		0.125				0.15	0.125	0.125		0.05					0.425
Grassland and dry shrubland	4						0.1	0.25			0.15					0.5
Desert	5	1														
Temperate Forest	6		0.3	0.2			0.2		0.25	0.05						
Boreal Forest	7			0.4	0.425					0.05			0.125			
Tundra	8												0.66	0.34		
Dry tundra	9															1
Ice	28	1														

0. Bare; Not vegetated;

1. M NET; Needleleaf evergreen temperate tree;

2. B NET; Needleleaf evergreen boreal tree;

3. B NDT; Needleleaf deciduous boreal tree;

4. T BET; Broadleaf evergreen tropical tree;

5. M BET; Broadleaf evergreen temperate tree;

6. T BDT; Broadleaf deciduous tropical tree;

7. M BDT; Broadleaf deciduous temperate tree;

8. B BDT; Broadleaf deciduous boreal tree;

9. M BES; Broadleaf evergreen shrub;

10. T BDS; Broadleaf deciduous tropical shrub;

11. B BDS; Broadleaf deciduous boreal shrub;

12. C3 Arc; C3 arctic grass;

13. C3 Gr; C3 non-arctic grass;

14. C4 Gr; C4 grass.

815 Globally averaged flux differences between our different model cases. All of the flux components are defined such that a positive number means that the specific component has a warming effect. Total fluxes are divided into their shortwave (SW) and longwave (LW) parts, which are then subdivided into more specific components. *Surf* and *top* denote the respective change in partial radiative balance at the surface and top of model, while *atm* and *clt* refer to the effect on of the clear atmosphere and integrated cloud cover.  $W\ m^{-2}$  Eoi:<sup>400</sup> - E<sup>280</sup> E<sup>1120</sup> - E<sup>280</sup> E<sup>280.P</sup> - E<sup>280</sup> E<sup>560</sup> - E<sup>280</sup> Eoi:<sup>280</sup> - E<sup>280</sup> Eoi:<sup>560</sup> - E<sup>560</sup> Eoi:<sup>560</sup> - Eoi:<sup>280</sup> SW<sub>surf</sub>

820 +7.19 +4.67 +0.26 +2.26 +6.56 +5.46 +1.17 SW<sub>top</sub> +6.81 +4.79 +0.07 +1.95 +5.80 +6.06 +2.21 SW<sub>atm</sub> -3.68 -4.72 +0.06 -2.15 -2.47 -2.71 -2.39 SW<sub>clt</sub> -1.00 -0.70 -0.23 -0.63 -1.19 +0.08 +0.64 LW<sub>surf</sub> -34.2 -45.3 +0.17 -20.0 -23.4 -24.8 -21.5 LW<sub>top</sub> -6.87 -4.64 -0.01 -1.79 -5.89 -6.27 -2.17 LW<sub>atm</sub> +14.8 +14.2 -0.13 +6.09 +11.3 +12.3 +7.04 LW<sub>clt</sub> +0.34 -1.02 +0.05 -0.39 +0.65 +0.24 -0.81

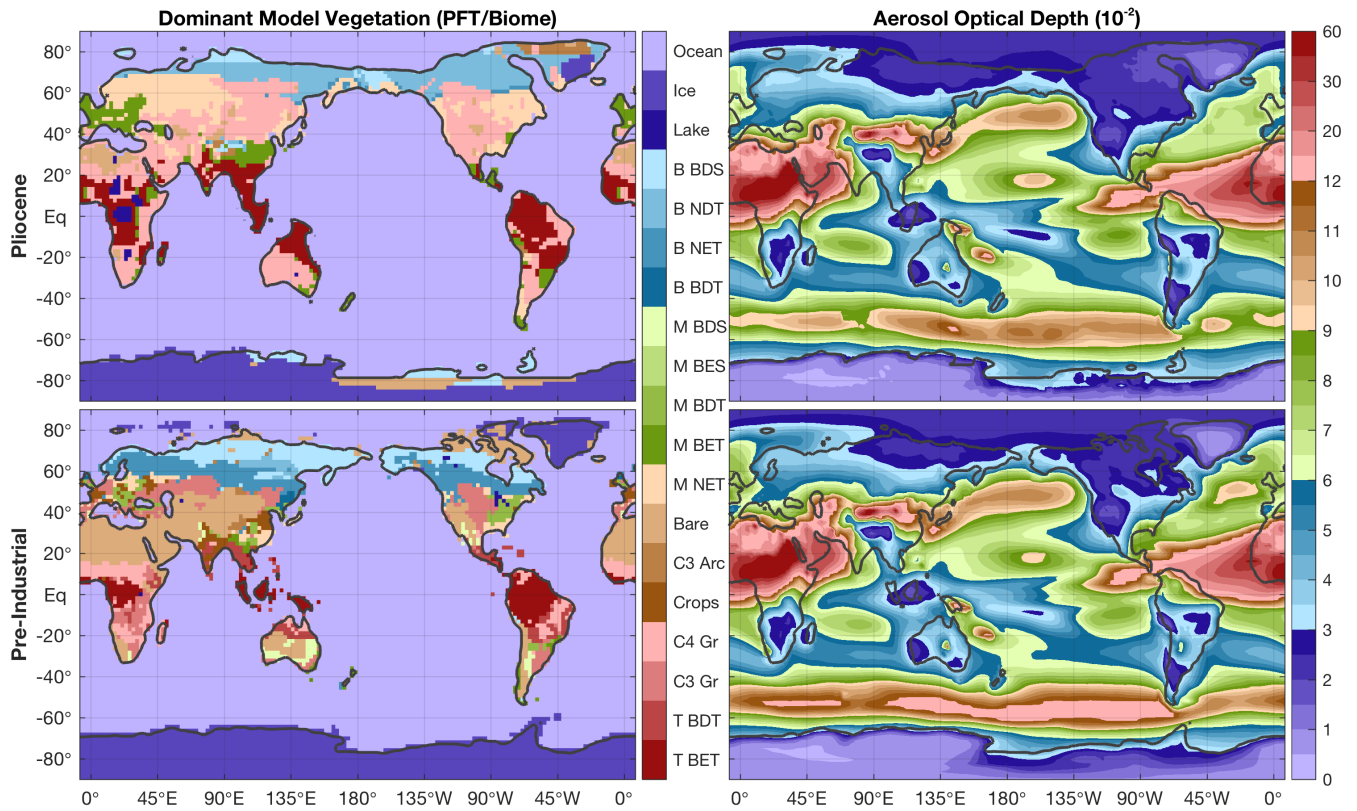


**Figure S1.** Pliocene (upper panels) and pre-industrial (lower panels) surface properties (left) and annual mean aerosol optical depth(right) in our model simulations. Vegetation is characterised by its dominant plant functional type, of which the used acronyms are given in Table S1.

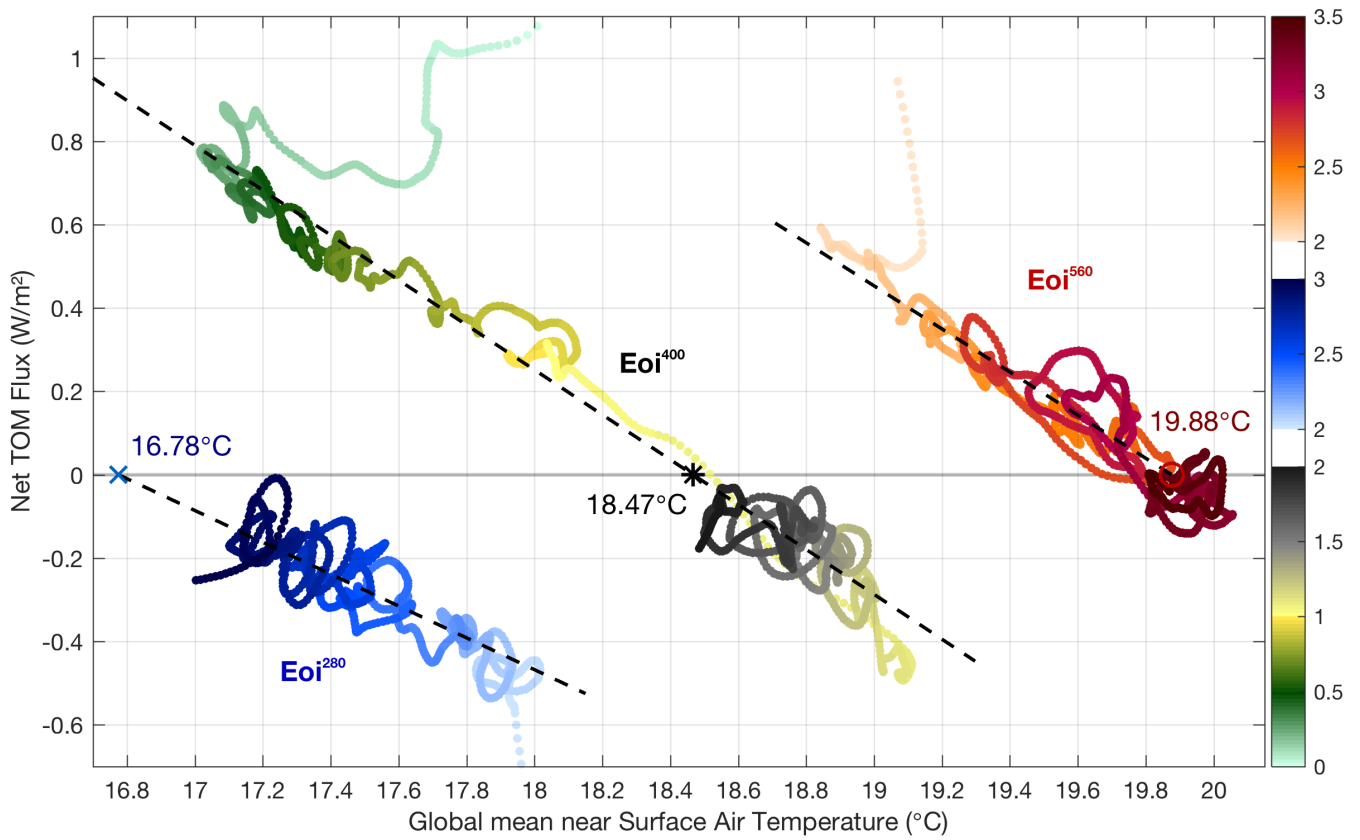


**Figure S2.** Full equilibration of our three Pliocene simulations: Eoi<sup>280</sup> (blue), Eoi<sup>400</sup> (green-yellow), and Eoi<sup>560</sup> (red), using the globally averaged annual mean near surface temperature and net top of model radiative flux. A 30-year smoothing average was applied to both time series, which are colour coded as a function of the model year (in kyr).

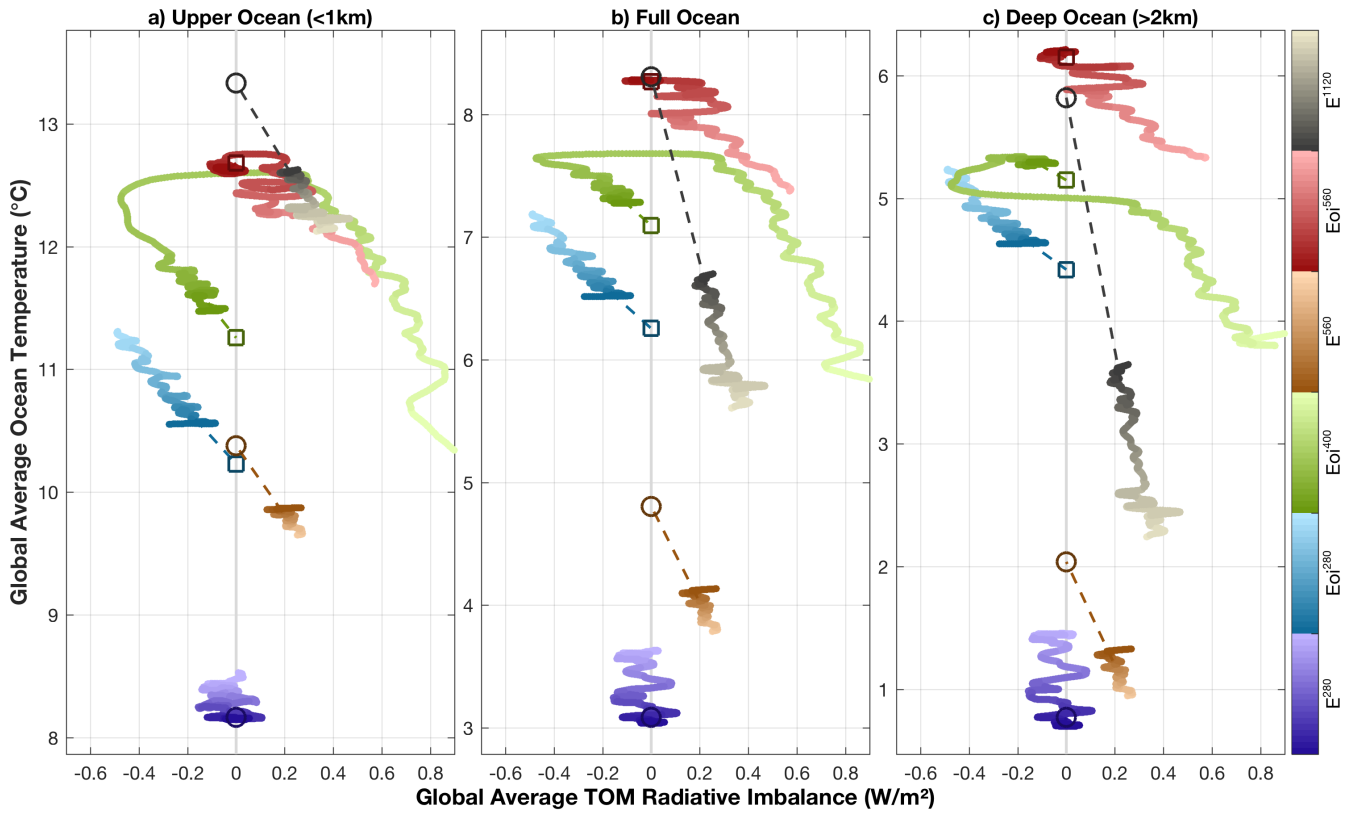


**Figure S3.** Full equilibration of our three standard pre-industrial ( $E^{280}$ ,  $E^{560}$ , and  $E^{1120}$ ) and Pliocene ( $Eoi^{280}$ ,  $Eoi^{400}$ , and  $Eoi^{560}$ ) cases, colour coded for the length of each simulation. As a function of annual mean, globally averaged top of model net radiative flux, we show **a)** upper (<1km), **b)** full depth, and **c)** deep (>2km) ocean average temperature. A 50-year smoothing average was applied to the time series, along with an extrapolation towards net radiative balance using a linear regression over the last 750 model years of each simulation.



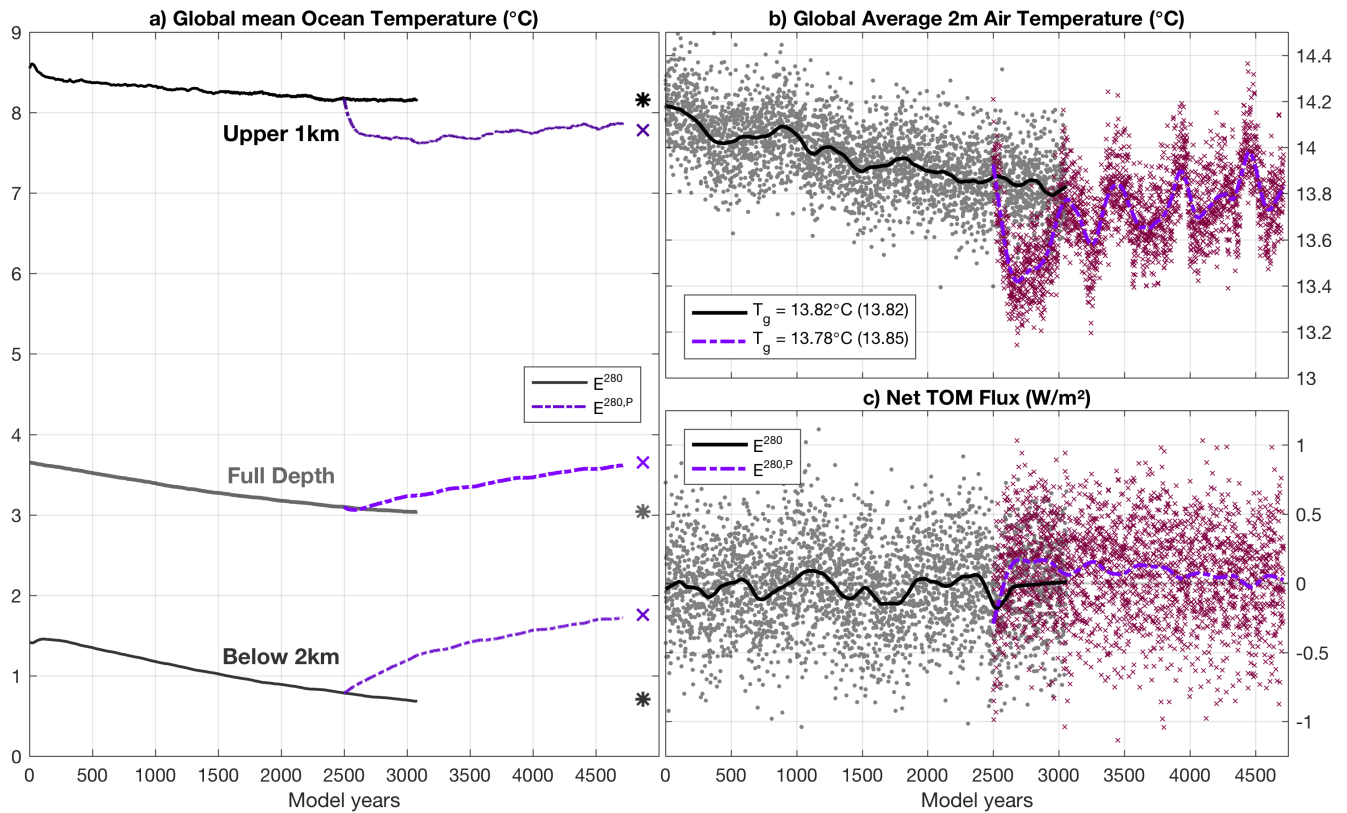


**Figure S4.** Time series of globally averaged temperatures for the entire length of our 2 main pre-industrial reference simulations:  $E^{280}$  (black), and  $E^{280,P}$  (purple). Shown are the **a)** upper (<1km; dark), deep (>2km; medium), and full depth (light) ocean temperature, **b)** near surface air temperature, and **c)** globally averaged top of model (TOM) net radiative flux. Thick lines in b,c show the corresponding time series after applying a 200-year smoothing mask. The estimated equilibrium temperatures are indicated at the end in a,b, using large markers and the same colour convention. The globally averaged, mean temperature ( $T_g$ ) over the last 100 years is added in the legend of b (bracketed values for the estimated equilibrium).

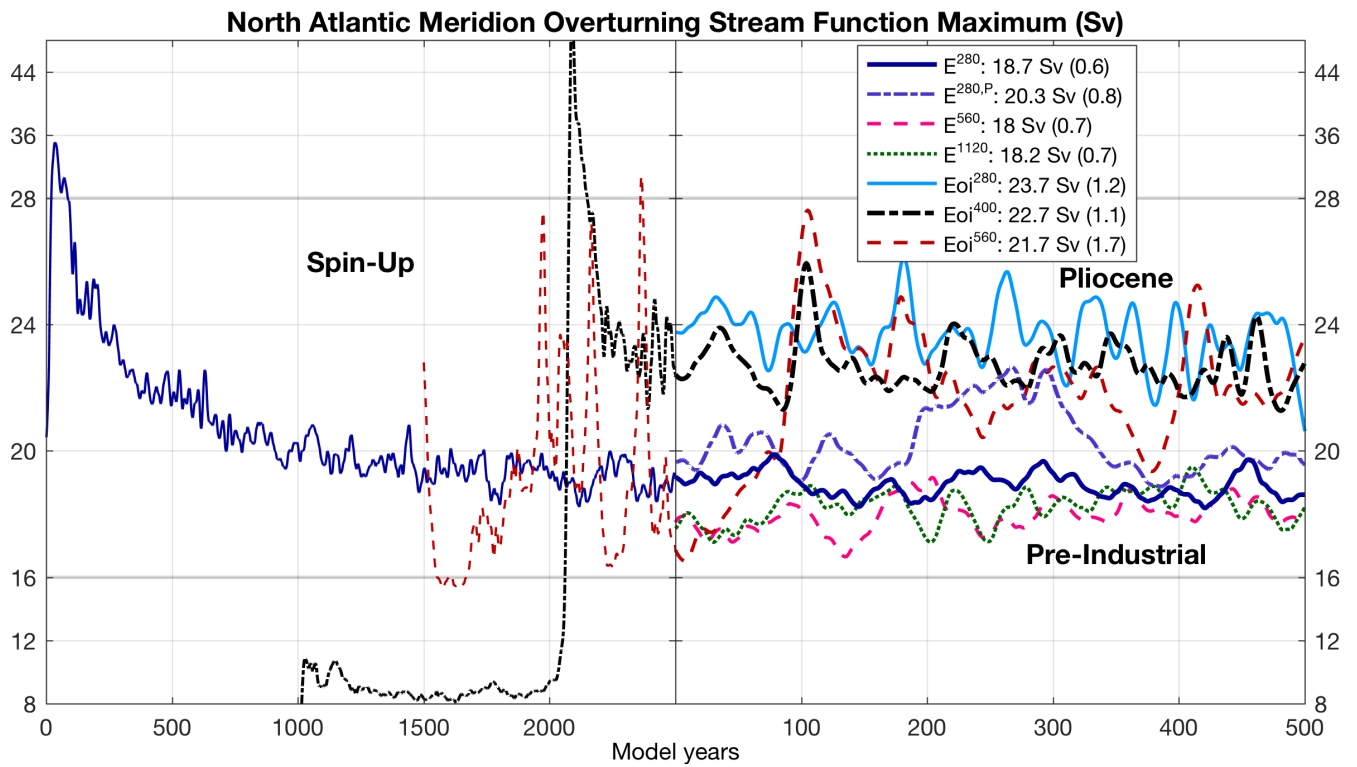


**Figure S5.** Time series of the annual mean AMOC strength (i.e. stream function maximum below 1km) for all 7 simulations, using a 20-year smoothing window. The last 500 years are aligned and shown in detail, with the full spinup of the  $E^{280}$ ,  $Eoi^{400}$ , and  $Eoi^{560}$  added on the left (note the different time scale). The average over the last 500 years is given in the legend for each case, with the corresponding standard deviation shown in brackets. Standard deviation is applied to the de-trended AMOC time series using a 250-year smoothing average.

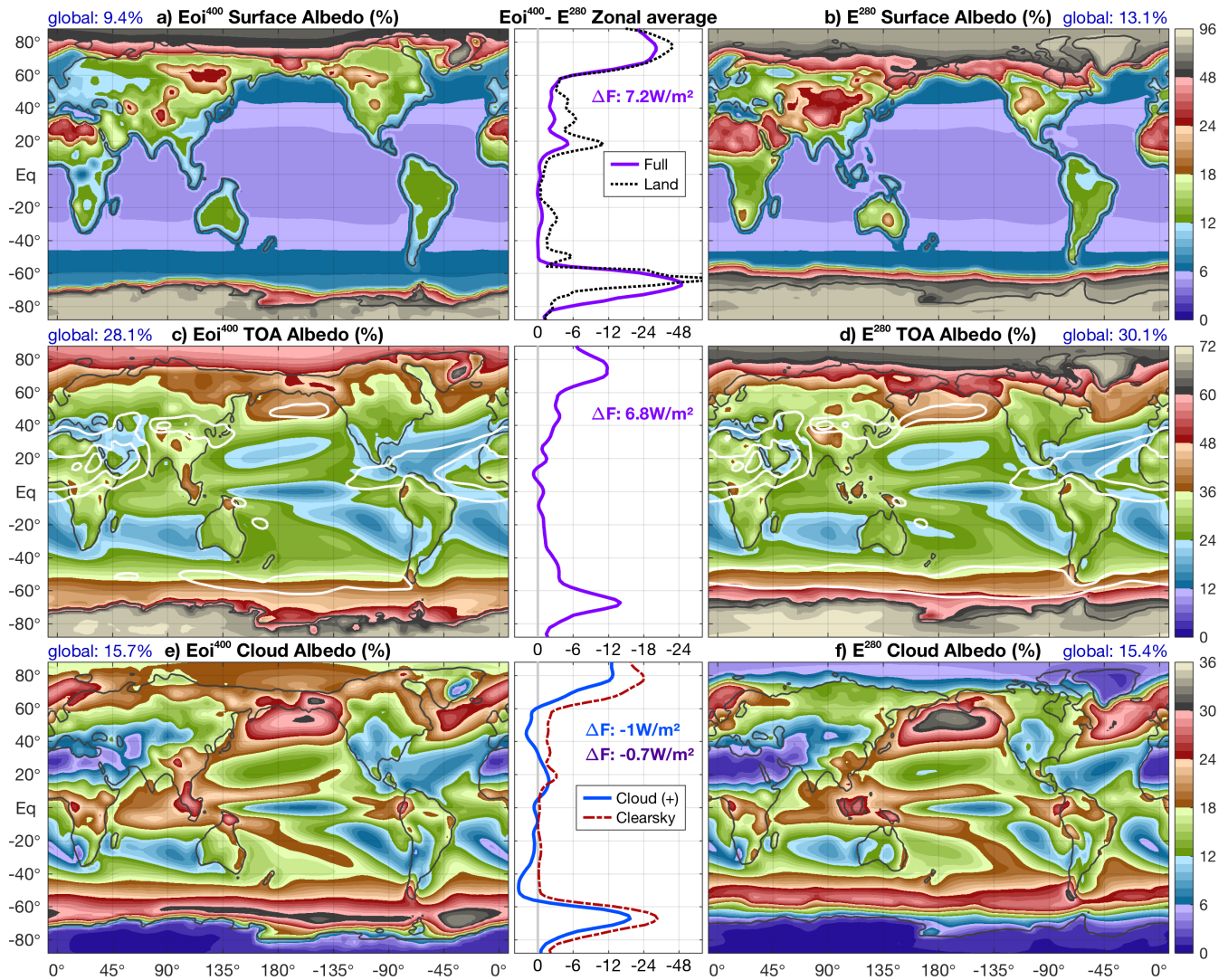


**Figure S6.** Annual mean albedo in the  $E^{280}$  (left) and  $E_{oi}^{400}$  (right) simulation, using the colour scales shown to the right. Shown from top to bottom are surface, top of atmosphere (TOA), and cloud albedo, with white contours in the TOA figures indicating aerosol optical depth at 0.1, 0.2, and 0.4 (see also Figure S1). The corresponding zonal average  $E_{oi}^{400} - E^{280}$  differences are given in the middle panels (note the negative scale; positive for cloud albedo). The resulting global average radiative forcing from each component is given, with the cloud forcing subdivided into shortwave-only (blue) and total (purple).

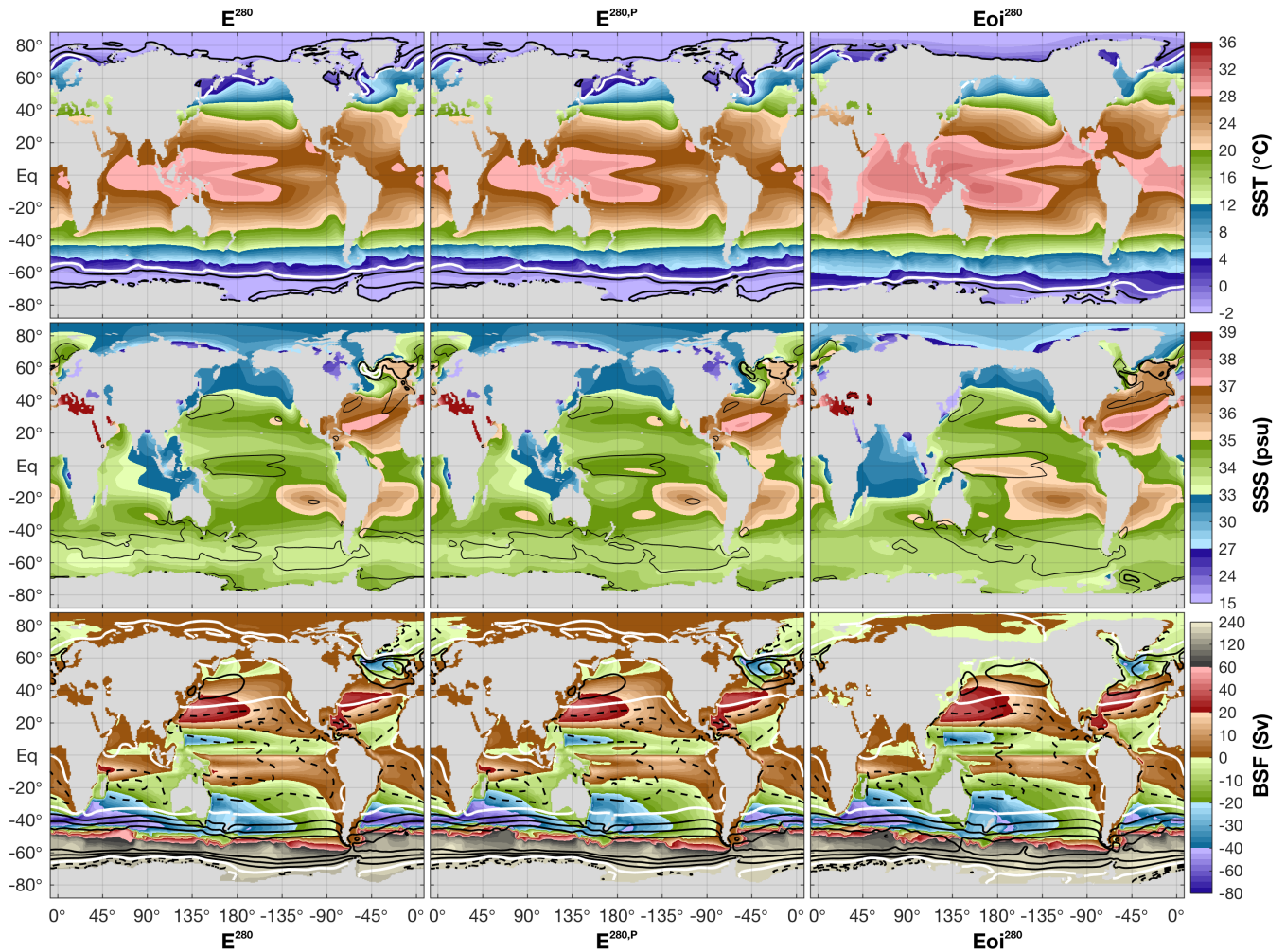


**Figure S7.** Annual mean oceanic fields from the (left to right)  $E^{280}$ ,  $E^{280,P}$ , and  $Eoi^{280}$  cases. **Top:** sea surface temperature (shading) and sea ice fraction (contours; white: 0.15, black: 0.5 and 0.9). **Middle:** Sea surface salinity (shading) and mixed layer depth (contours; black: 100m, thick black: 250m, thick white: 500m). **Bottom:** Barotropic stream function (BSF; shading) and zonal wind stress (contours every  $5 \cdot 10^{-2}$  Pa, dashed:  $<0$ , thick white line at 0 Pa).

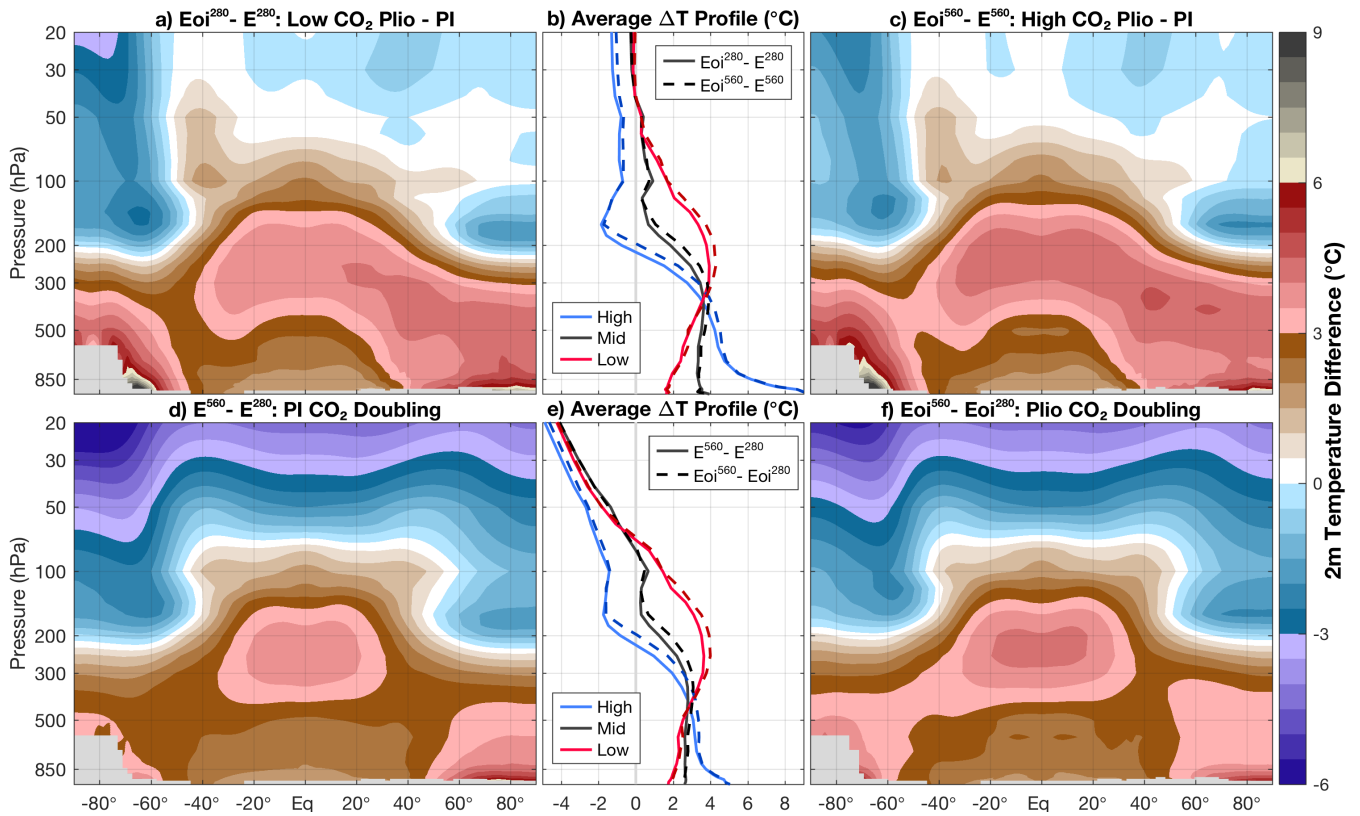


**Figure S8.** Annual mean, zonally averaged air temperature difference as a function of pressure, between our four *sensitivity* simulations; **a)**  $Eoi^{280} - E^{280}$ , **c)**  $Eoi^{560} - E^{560}$ , **d)**  $E^{560} - E^{280}$ , and **f)**  $Eoi^{560} - Eoi^{280}$ . **b)** Average vertical temperature difference profile of  $Eoi^{280} - E^{280}$  (solid) and  $Eoi^{560} - E^{560}$  (dashed) for high ( $>60^\circ$ ; blue), middle ( $30-60^\circ$ ; black), and low ( $<30^\circ$ ; red) latitudes. **e)** As in b, but for  $E^{560} - E^{280}$  (solid) and  $Eoi^{560} - Eoi^{280}$  (dashed).

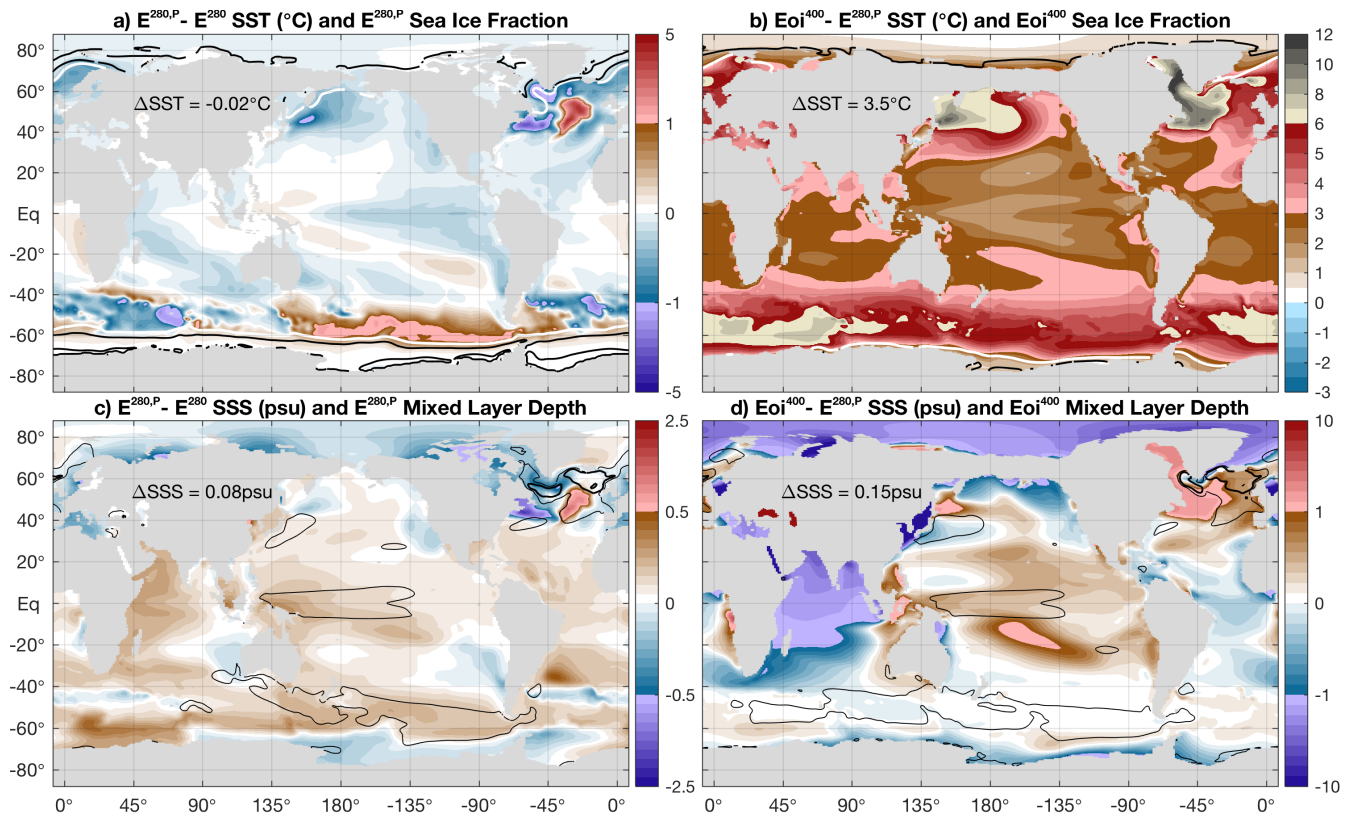


**Figure S9.** Annual mean SST difference between **a)**  $E^{280,P} - E^{280}$ , and **b)**  $E_{oi}^{400} - E^{280,P}$ . The global average difference ( $\Delta\text{SST}$ ) is given, contours show  $E^{280,P}$  (a) and  $E_{oi}^{400}$  (b) annual mean sea ice fraction (white: 15%, cyan: 50%, and black: 90%). **c,d)** As in a,b but for sea surface salinity difference (shading) and mixed layer depth (contours; black: 100m, thick black: 250m, and white: 500m).

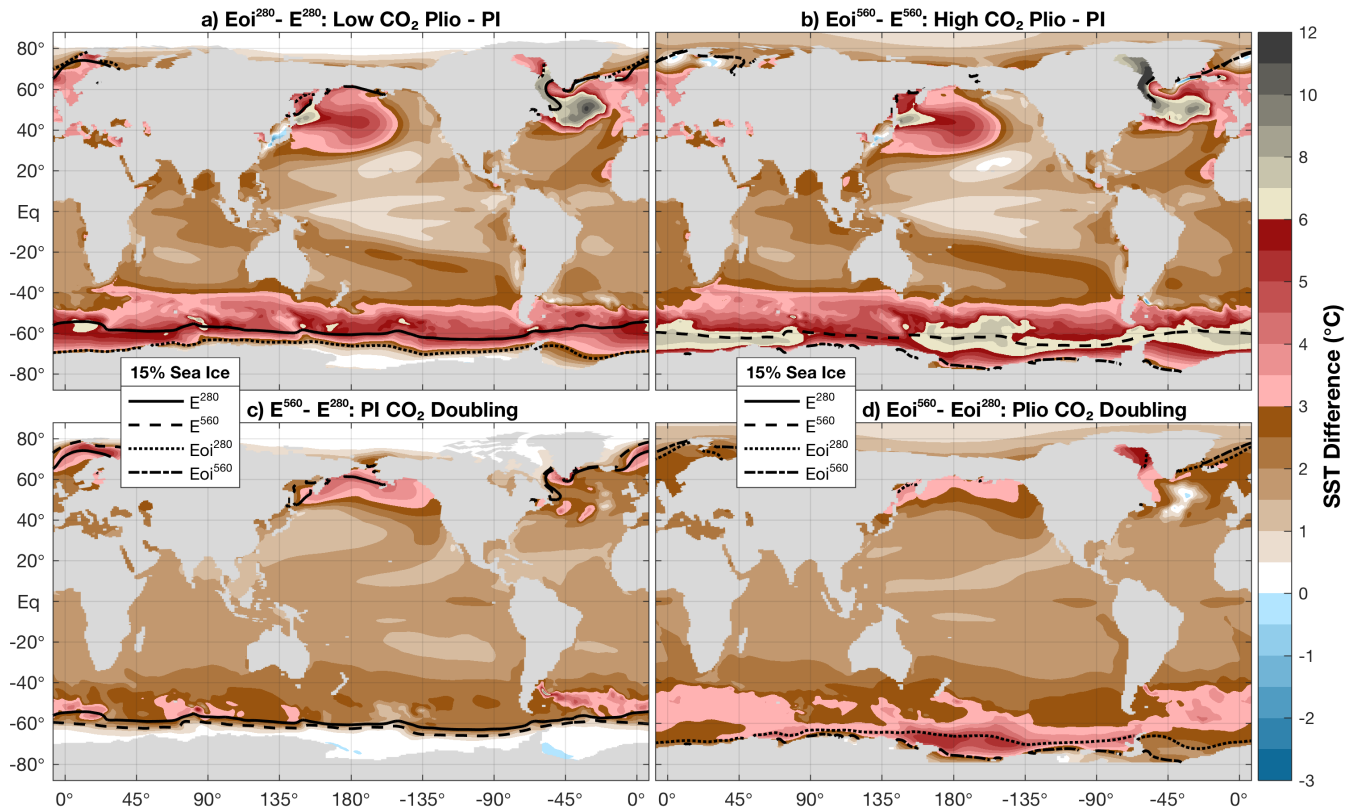


**Figure S10.** Zonally-averaged near-Annual mean sea surface air temperature (SST) difference of each model case from the between our four sensitivity simulations: **a)**  $E_{oi}^{280} - E^{280}$  pre-industrial-reference, with the zonal-variation (10 and 90 percentiles) of the **b)**  $E_{oi}^{560} - E^{560}$ , **c)**  $E^{560} - E^{280}$  indicated, and **d)**  $E_{oi}^{560} - E_{oi}^{280}$ . Contours showing the annual mean sea ice edge (i.e. 0.15 ice fraction) in gray shading black; solid:  $E^{280}$ , dashed:  $E^{560}$ , dotted:  $E_{oi}^{280}$ , and dash-dotted:  $E_{oi}^{560}$  (2 shown per panel).

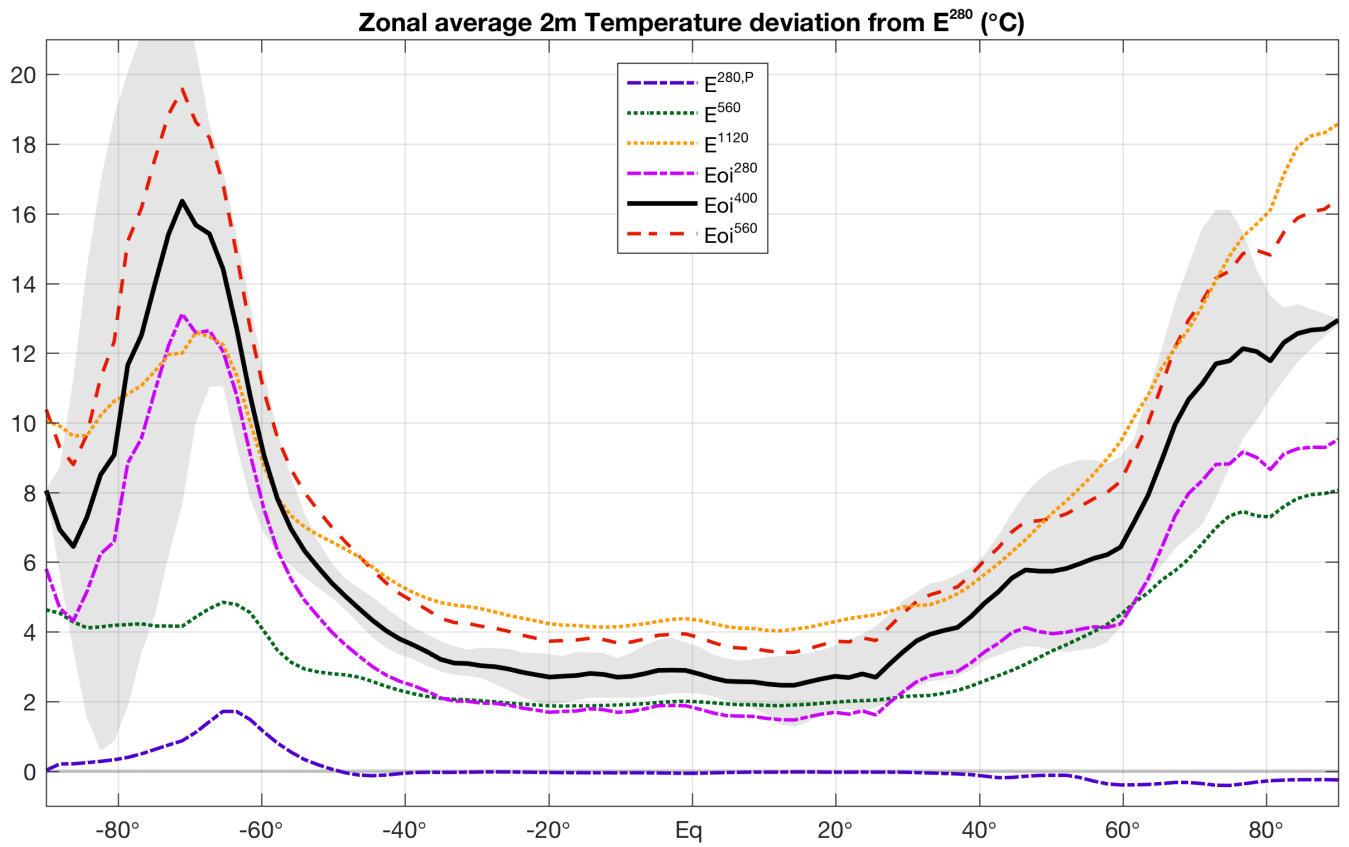


**Figure S11.** Zonally averaged near surface air temperature difference of each model case from the  $E^{280}$  pre-industrial reference, with the zonal variation (10 and 90 percentiles) of the  $EoI^{400} - E^{280}$  indicated in gray shading.



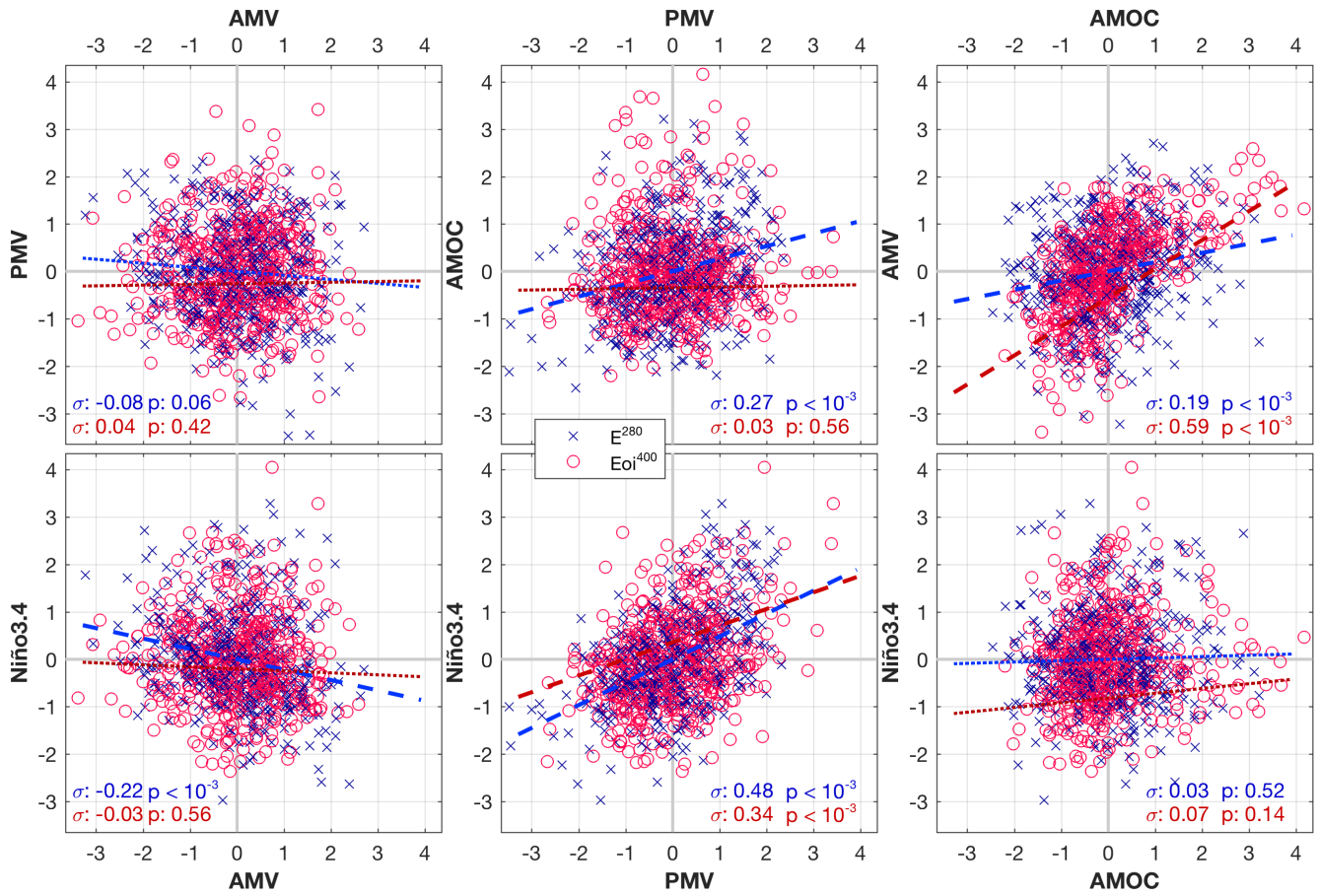


**Figure S12.** Scatter plots of annual mean AMV, PMV, AMOC, and Niño 3.4 indices of the  $E^{280}$  (blue crosses) and  $E_{oi}^{400}$  (red circles) using 500 years of SST data. Cross correlations between the different indices are given along with their p-value. Coloured lines in corresponding colours for each simulation show a linear regression, with thick dashed lines used for statistically significant correlations (i.e. p-value  $< 0.05$ ).